

Direct Observation of Chirality-Induced Spin Selectivity in Electron Donor-Acceptor Molecules

Hannah J. Eckvahl,^{1†} Nikolai A. Tcyrulnikov,^{1†} Alessandro Chiesa,^{2†} Jillian M. Bradley,¹ Ryan M. Young,¹ Stefano Carretta,^{2*} Matthew D. Krzyaniak,^{1*} and Michael R. Wasielewski^{1*}

¹Department of Chemistry, Center for Molecular Quantum Transduction, and Paula M. Trienens Institute for Sustainability and Energy, Northwestern University, Evanston, IL 60208-3113 USA.

²Università di Parma, Dipartimento di Scienze Matematiche, Fisiche e Informatiche, Parma, I-43124, Italy.

*Corresponding authors. Email: m-wasielewski@northwestern.edu; mdkrzyaniak@northwestern.edu; stefano.carretta@unipr.it

†These authors contributed equally to this work

One-Sentence Summary: The spin dynamics of photogenerated radical pairs are strongly influenced by molecular chirality.

Abstract:

The role of chirality in determining the spin dynamics of photoinduced electron transfer in donor-acceptor molecules remains an open question. Although chirality-induced spin selectivity (CISS) has been demonstrated in molecules bound to substrates, experimental information about whether this process influences spin dynamics in the molecules themselves is lacking. Here we use time-resolved electron paramagnetic resonance spectroscopy to show that CISS strongly influences the spin dynamics of isolated covalent donor-chiral bridge-acceptor (D-B χ -A) molecules in which selective photoexcitation of D is followed by two rapid, sequential electron transfer events to yield D⁺-B χ -A⁻. Exploiting this phenomenon affords the possibility of using chiral molecular building blocks to control electron spin states in quantum information applications.

Molecules offer a wide variety of quantum properties that could potentially be exploited in qubit architectures for quantum information science (QIS).^(1, 2) Moreover, molecules afford the ability to tailor these properties as applications dictate, while controlling structure with atomic precision. One such property of growing interest is molecular chirality, which plays an essential role in many chemical reactions and nearly all biological processes. Naaman, Waldeck, and coworkers presented evidence of the relationship between molecular chirality and electron spin^(3, 4) when they observed that electrons photoemitted from a gold surface coated with a thin film of DNA have a preferred spin state, a phenomenon now known as chirality-induced spin selectivity (CISS).⁽⁵⁾ Subsequent experiments using molecules bound to metallic, semiconductor, or magnetic substrates have confirmed a connection between electron motion and spin projection along the chiral axis, which is selected to be parallel or antiparallel to the motion, depending on the handedness of the chiral molecule.⁽⁵⁻⁹⁾ The spin selectivity of the effect can be very high, even at room temperature, and its theoretical foundations are still being explored.⁽¹⁰⁻¹⁷⁾ However, a key problem hindering a fundamental understanding of CISS is that it is difficult to separate the role of the substrate from that of the chiral molecule.

Hence, it is crucial to investigate how CISS affects electron spin dynamics in molecules undergoing electron transfer that are not bound to substrates. Achieving this understanding would make it possible to design chiral molecular building blocks to manipulate electron spin states, which has potential for QIS applications. In particular, the occurrence of CISS at the molecular level has been proposed as an enabling technology for quantum applications, e.g. solving key issues like single-spin readout and high-temperature spin qubit initialization.⁽⁶⁾

Here we show direct evidence of CISS in isolated covalent donor-chiral bridge-acceptor (D-B χ -A) molecules in which selective photoexcitation of D to its lowest excited singlet state (¹*D) is followed by two rapid, sequential electron transfer events: ¹*D-B χ -A \rightarrow D⁺-B χ ⁻-A \rightarrow D⁺-B χ -A⁻ (Fig. 1A). If formation of D⁺-B χ -A⁻ occurs in $\lesssim 1$ ns, the resulting entangled electron spin pair is prepared initially in a nearly pure singlet state, ¹(D⁺-B χ -A⁻). These states are commonly referred to as spin-correlated radical pairs (SCRPs) and have been studied in systems ranging from photosynthetic proteins⁽¹⁸⁻²¹⁾ and related model systems⁽²²⁻²⁵⁾ to DNA hairpins.⁽²⁶⁻³⁰⁾ However, in all these cases, no consideration was given to the possible influence of chirality on the SCRPs spin dynamics.

To demonstrate the occurrence of CISS, we have synthesized pairs of covalent D-B χ -A enantiomers, (*R*)-**1-h₉** (-**d₉**) and (*S*)-**1-h₉** (-**d₉**), where D is either non-deuterated (-**h₉**) or fully deuterated (-**d₉**) *peri*-xanthenoxanthene,⁽³¹⁾ B χ is a pair of naphthalene-1,8-dicarboximides that are linked at their 4-positions to form an enantiomeric pair of axially chiral dimers (*R*)-NMI₂ and (*S*)-NMI₂⁽³²⁾ and A is naphthalene-1,8:4,5-bis(dicarboximide) (NDI) (see Supplementary Materials, figs. S1-S2). The structures of (*R*)-**1-h₉** (-**d₉**) and (*S*)-**1-h₉** (-**d₉**) and the corresponding achiral reference molecules **2-h₉** (-**d₉**) are shown in Fig. 1B. The enantiomers were separated using HPLC with a chiral stationary phase (fig. S3) and their circular dichroism spectra are given in fig. S4. We have characterized the charge separation and recombination dynamics of these molecules using transient optical absorption (TA) spectroscopy and the CISS effect on their spin dynamics using time-resolved EPR spectroscopy using either continuous (TREPR) or pulsed microwave radiation (pulse-EPR).

We find that CISS yields characteristic features in the TREPR spectra of the photogenerated PXX⁺-NMI₂-NDI⁻ SCRPs in (*R*)-**1-h₉** (-**d₉**) and (*S*)-**1-h₉** (-**d₉**), which are absent in achiral **2-h₉** (-**d₉**), when the direction of electron transfer is oriented orthogonal to the applied static magnetic

field direction in agreement with simulations. Conversely, the corresponding spectra of PXX^+ - NMI_2 - NDI^- are practically identical when the field is parallel to the electron transfer direction.

Time-resolved EPR Spectroscopy

Samples of (*R*)-**1-h₉** (**-d₉**), (*S*)-**1-h₉** (**-d₉**), and **2-h₉** (**-d₉**) were each prepared in the nematic liquid crystal 4-cyano-4'-(*n*-pentyl)biphenyl (5CB), which was aligned in a magnetic field at 295 K, then rapidly frozen to 85 K, which aligns the long axes of these molecules along the magnetic field. The orientation of the molecules aligned in frozen 5CB can then be rotated relative to the applied magnetic field direction. Since solid 5CB is an optically scattering medium, to assess the photo-driven charge separation dynamics of these molecules at low temperature, we employed both femtosecond and nanosecond transient optical absorption spectroscopy substituting glassy butyronitrile for 5CB at 105 K. Transient absorption spectra and kinetics are given in figs. S5 and S6. The data show that in each case ultrafast two-step charge separation occurs in $\lesssim 0.2$ ns to give PXX^+ - NDI^- , which recombines to its ground state in $\tau = 46\text{-}66$ μs , providing ample time for TREPR measurements. The presence of a ~ 0.35 T static magnetic field in the TREPR experiments does not affect the ultrafast electron transfer reactions because the Zeeman interaction (~ 0.3 cm^{-1}) at that field strength is much less than the adiabatic energy gaps ($\sim 20\text{-}80$ cm^{-1}) for these reactions (see table S1 and SM for details).

Pulse-EPR techniques were used to assess the quality of the alignment of (*R*)-**1-h₉** (**-d₉**), (*S*)-**1-h₉** (**-d₉**), and **2-h₉** (**-d₉**) 5CB by measuring the isotropic exchange (J) and dipolar (D) spin-spin interactions for their photogenerated SCRPs, where $D(\theta) = d(1 - 3 \cos^2 \theta)$ and $d = 52.04 \text{ MHz} \cdot \text{nm}^3 / r_{DA}^3$ in the point dipole approximation, which gives detailed distance and orientation information as defined by the Hamiltonian in eq. S3. If photogeneration of the SCRPs is followed by a Hahn echo microwave pulse sequence: $\pi/2$ pulse - delay τ - π pulse - delay τ - spin echo, and the time delay τ is scanned, coherent oscillations between the eigenstates of the SCRPs Hamiltonian $|\Phi_A\rangle$ and $|\Phi_B\rangle$ (see below) that are related to both J and $D(\theta)$ modulate the spin echo amplitude.^(21, 33-37) When this experiment is performed on spin-coherent SCRPs, the echo appears out-of-phase, *i.e.*, in the detection channel in quadrature to the one in which it is expected, and is therefore termed out-of-phase electron spin echo envelope modulation (OOP-ESEEM).^(21, 33-37) For large SCRPs distances, r_{DA} , J can be neglected and the OOP-ESEEM oscillation frequency is approximately $2d$ when $\theta = 0^\circ$ and d when $\theta = 90^\circ$. Thus, OOP-ESEEM can be used to measure SCRPs distances for a given angle of the dipolar axis relative to the magnetic field.^(28, 36-38) The dipolar axis in SCRPs connects the centroids of the spin distributions of the two radicals. Figures S7 and S8 show the OOP-ESEEM data for (*R*)-**1-h₉** (**-d₉**), (*S*)-**1-h₉** (**-d₉**), and **2-h₉** (**-d₉**) assuming that their dipolar axes are aligned parallel or perpendicular to the magnetic field. Fitting the OOP-ESEEM data shows that the measured PXX-h_9^+ - NDI^- distances of (*R*)-**1-h₉**, (*S*)-**1-h₉**, and **2-h₉** are 2.48 ± 0.01 , 2.48 ± 0.01 , and 2.28 ± 0.01 nm, respectively, while the corresponding PXX-d_9^+ - NDI^- distances of (*R*)-**1-d₉**, (*S*)-**1-d₉**, and **2-d₉** are 2.53 ± 0.01 , 2.51 ± 0.01 , and 2.29 ± 0.02 nm, respectively (table S2). These experimental distances are consistent with the center-to-center distances between PXX and NDI determined from density functional theory calculations on (*R*)-**1-h₉**, (*S*)-**1-h₉**, and **2-h₉**, where $r_{DA} = 2.59$, 2.60 , and 2.40 nm, respectively (fig. S9 and tables S3-S5). The agreement between the experimental and calculated distances shows that the D^+ - $\text{B}\chi$ - A^- SCRPs are well-aligned along the magnetic field direction in frozen 5CB.

The TREPR spectra of aligned (*R*)-**1-h₉**, (*S*)-**1-h₉**, and **2-h₉** were obtained by photoexciting the samples with a 450 nm, 7 ns laser pulse and monitoring the magnetization with continuous microwaves using direct detection (see SM). The spectra obtained 100 ns after the laser pulse (T_{DAF}) are shown in Fig. 2. When the long axes of these molecules are aligned parallel to the

magnetic field direction ($\theta = 0^\circ$), both enantiomers as well as the achiral reference molecule give the same spectra (Figs. 2A and 2C). Rotating the samples so that the long axes of (*R*)-**1-h₉**, (*S*)-**1-h₉**, and **2-h₉** are aligned perpendicular to the magnetic field direction ($\theta = 90^\circ$), results in the appearance of outer wings in the spectra of chiral (*R*)-**1-h₉** and (*S*)-**1-h₉** (Fig. 2B). No such enhancement is observed for achiral **2-h₉**. As explained below, we posit that these new features result from the contribution of CISS to the formation of the SCRPs in (*R*)-**1-h₉** and (*S*)-**1-h₉**. Deuteration of PXX⁺ narrows the overall linewidth of (*R*)-**1-d₉**, (*S*)-**1-d₉**, and **2-d₉**, while retaining the same orientation dependence of the signal (Figs. 2C and 2D).

Effect of CISS on Radical Pair Spin Dynamics

In the molecules described here, the D⁺-A⁻ distances are ≥ 23 Å, so that the spin-spin interactions J and D are small relative to the ~ 0.35 T applied magnetic field. Thus, the Zeeman term is by far the leading term in the SCRPs spin Hamiltonian (eq. S3), so that the SCRPs wavefunctions $|S\rangle = \frac{1}{\sqrt{2}} (|\uparrow\downarrow\rangle - |\downarrow\uparrow\rangle)$ and $|T_0\rangle = \frac{1}{\sqrt{2}} (|\uparrow\downarrow\rangle + |\downarrow\uparrow\rangle)$, which are magnetic field invariant, remain close in energy, while $|T_{+1}\rangle = |\uparrow\uparrow\rangle$ and $|T_{-1}\rangle = |\downarrow\downarrow\rangle$ are well separated in energy from both $|S\rangle$ and $|T_0\rangle$. In particular, both $|T_{+1}\rangle$ and $|T_{-1}\rangle$ are eigenstates of the spin Hamiltonian, while $|S\rangle$ and $|T_0\rangle$ are not eigenstates because of the different electronic g -factors and hyperfine fields of the two spins. Coherent mixing of $|S\rangle$ and $|T_0\rangle$ yields $|\Phi_A\rangle = \cos\phi |S\rangle + \sin\phi |T_0\rangle$ and $|\Phi_B\rangle = -\sin\phi |S\rangle + \cos\phi |T_0\rangle$ (Fig. 3A), which are eigenstates of the spin Hamiltonian, where the angle ϕ in the mixing coefficients is derived from the magnetic parameters of the SCRPs (see SM).(39-41)

In the ultrafast electron transfer regime observed here, the initial spin state for an achiral SCRPs is the entangled singlet $|S\rangle$ state yielding populations only on $|\Phi_A\rangle$ and $|\Phi_B\rangle$. Therefore, four allowed transitions occur between them and the initially unpopulated $|T_{+1}\rangle$ and $|T_{-1}\rangle$ states, giving rise to a spin-polarized (out of equilibrium) EPR spectrum. When $\theta = 0^\circ$, this results in a typical (*e, a, e, a*) spin polarization pattern (low to high field, where *a* = enhanced absorption, and *e* = emission) because $D(\theta) < 0$. (39-41) Conversely, when $\theta = 90^\circ$, the pattern is reversed (*a, e, a, e*) because $D(\theta) > 0$. Since the g -tensors of PXX⁺ and NDI⁻ are very similar, i.e. [2.0045, 2.0045, 2.0031](42) and [2.0047 2.0047 2.0027],(43) respectively, the expected SCRPs polarization patterns, (*e, a, e, a*) or (*a, e, a, e*), are reduced to broadened (*e, a*) or (*a, e*) patterns, as observed experimentally for the achiral reference molecules **2-h₉** and **2-d₉** (Fig. 2, blue traces). Our OOP-ESEEM results show that the dipolar axis of each SCRPs is well aligned with the long axis of each molecule so that the dipolar axis and the chirality axis of (*R*)-**1-h₉** (**-d₉**) and (*S*)-**1-h₉** (**-d₉**) are nearly parallel. The angle θ between this axis and the applied magnetic field (B_0) direction is depicted in Fig. 3B for the parallel and in Fig. 3E for perpendicular orientations. CISS mixes triplet character into the initial singlet SCRPs, thus the initial populations of $|\Phi_A\rangle$, $|\Phi_B\rangle$, $|T_{+1}\rangle$ and $|T_{-1}\rangle$ and the corresponding transition intensities are predicted to change as well.(44-47) If CISS is the sole contribution to the spin dynamics and $\theta = 0^\circ$ (Fig. 3D), the state following electron transfer would be $|\uparrow\downarrow\rangle$ or $|\downarrow\uparrow\rangle$, depending on the chirality of the enantiomer and whether B_0 is parallel or antiparallel to the electron motion. Given that the typical alignment of linear D-B-A molecules within nematic liquid crystals is not unidirectional, B_0 has equal probability of being parallel or antiparallel to the electron motion and hence, if coherences are lost, the initial state is an equal mixture of $|\uparrow\downarrow\rangle$ and $|\downarrow\uparrow\rangle$, and is thus equivalent to having a pure initial $|S\rangle$ state. This situation is shown schematically in Fig. 3C, where the blue and red traces depict the idealized TREPR spectra expected when CISS contributes 0 and 100%, respectively. Indeed, the observed spectra of both

enantiomers as well as the achiral reference molecule are practically identical for $\theta = 0^\circ$ (Figs. 2A and 2C).

In contrast, when the chirality axis is orthogonal to B_0 (Fig. 3E) the initial state is very different in the presence or absence of CISS. In particular, the CISS contribution initially populates $|T_{+1}\rangle$ and $|T_{-1}\rangle$ (see eq. S12). Therefore, if the SCRCP spin state has a 100% CISS contribution, the TREPR spectra have a nearly opposite intensity pattern with respect to the case in which CISS does not contribute. This is illustrated in Fig. 3F where the blue and red lines in the idealized TREPR spectra correspond to the intensity for the pure $|S\rangle$ (I_S) and pure CISS (I_{CISS}) initial conditions, respectively.

Starting from recent theoretical models(44-47) describing the influence of CISS on SCRCP spin dynamics in cases for which the CISS contribution will not be 100%, the initial state will be a superposition or a mixture of $|S\rangle$ and $|T_0\rangle$ along the chiral axis direction, making the detection of CISS less obvious. In fact, the spectral line intensities in this case are the weighted sum of I_S and I_{CISS} , which occur at the same resonance fields and tend to cancel out (see details in the SM). The key to unraveling CISS and pure singlet contributions to the SCRCP spin state in the molecules studied here is the observation of a larger EPR linewidth that occurs when CISS contributes. Indeed, the sum of the two contributions (Fig. 3F, black trace) yields a signal that displays lateral wings of opposite sign and central features that are narrower than those produced in the absence of CISS, exactly as observed experimentally in Figs. 2B and 2D. These features are unambiguous signatures of CISS, because they cannot be produced starting from an initial $|S\rangle$ state, where the polarization pattern is fixed to (a, e) for $\theta = 90^\circ$ by the sign of $D(\theta)$.(39-41)

The larger linewidth obtained for the CISS initial state arises from the very different dependence of I_S and I_{CISS} on the degree of coherent mixing in the eigenstates. Indeed, $|I_{CISS}|$ increases with increasing entanglement ($\phi \rightarrow 0$) while $|I_S|$ decreases (fig. S10). Exploring the variation of the intensity by varying the composition of the $|\Phi_A\rangle$ and $|\Phi_B\rangle$ eigenstates is made possible by the presence of several nuclear spins and by distributed magnetic parameters, e.g. dipolar couplings, often termed strain. Therefore, moving from the center of each transition, i.e. the center of the distributions of the magnetic parameters and hyperfine fields, to the tail of the lineshape corresponds to changing the composition of the eigenstates, producing different linewidths for different initial states. If entanglement in the eigenstates is larger in the tails of the spectrum, the CISS contributions result in magnetic field dependent broadening, giving rise to lateral contributions to the lineshape of opposite sign with respect to the central features (Fig. 3F, black trace).

To confirm this interpretation, we consider the spectra of partially deuterated (*R*)-**1-d₉** and (*S*)-**1-d₉**. By strongly diminishing the hyperfine couplings on one of the two radicals, we change the distribution of the eigenstate composition and probe its effect on the lineshape. The measured spectra for $\theta = 0^\circ$ and $\theta = 90^\circ$ are shown in Figs. 2C and 2D, respectively. While no qualitative effect is visible in the parallel direction as expected, the lateral wings are significantly reduced in the perpendicular orientation. These spectra were simulated using a minimal SCRCP model with either one spin- $\frac{1}{2}$ nucleus (hydrogen atom) on both NDI $^-$ and PXX $^+$ or only on NDI $^-$, the latter of which is the partially deuterated case. For reasonable values of the hyperfine couplings, the simulations shown in Fig. 4 reproduce the experimental behavior.

The intensities of the lateral wings are correctly reproduced by combining I_S and I_{CISS} with weights of 41% and 59%, respectively (Fig. 4). While a 59% CISS contribution is remarkable, it must be stressed that this is a minimal model in which the effect of the nuclei is accounted for only qualitatively and a full spectral simulation with all nuclear spins in the fully protonated molecules is very demanding. However, we have been able to perform the simulation for the deuterated case,

which includes all four ^1H and two ^{14}N nuclei coupled to the electron spin in $\text{NDI}^{\bullet-}$ and effects of dipolar strain. In this case, the experimental behavior is very well reproduced with a 47% CISS contribution, which is still considerable.

Further evidence for the validity of this interpretation is obtained by investigating the time dependence of the TREPR spectra, which reflect the time evolution of the $\text{D}^{\bullet+}\text{-B}\chi\text{-A}^{\bullet-}$ spin states under the combined effect of coherent and incoherent terms as described by the stochastic Liouville equation and the presence of the microwave field (see SM). Indeed, figs. S11 and S12 show that the dependence of the observed intensity of the wings of the spectra are similar to that of the main peaks, in agreement with our numerical simulations.

Interestingly, the CISS contribution to the spin dynamics of (*R*)-**1-h₉** (**-d₉**) and (*S*)-**1-h₉** (**-d₉**) is similar to the ~50% spin polarization recently reported for an axially chiral binaphthalene derivative covalently linked to a gold film deposited on nickel.⁽⁴⁸⁾ While this single comparison suggests that the observed CISS effect for the binaphthalene attached to the gold surface may be largely due to the chiral molecule, additional comparative work is needed on a variety of systems to warrant such a conclusion.

Conclusions

We have found direct evidence of the CISS effect on the spin dynamics of photogenerated radical ion pairs in molecular electron donor-acceptor molecules. The observation of CISS in these systems affords possibilities both for increasing our understanding of this important phenomenon and for its possible applications. Importantly, these results show that the substrates/electrodes with their possibly large spin-orbit couplings are not needed for CISS to occur and that TREPR spectroscopy can directly access the spin dynamics resulting from CISS. This provides key information to guide theoretical investigations and makes possible many new targeted experimental studies. In addition, observing CISS at the molecular level is the first step required to transform this fundamental phenomenon into an enabling technology for quantum applications.

References and Notes

1. M. Atzori, R. Sessoli, The second quantum revolution: Role and challenges of molecular chemistry. *J. Am. Chem. Soc.* **141**, 11339-11352 (2019).
2. M. R. Wasielewski *et al.*, Exploiting chemistry and molecular systems for quantum information science. *Nat. Rev. Chem.* **4**, 490-504 (2020).
3. K. Ray, S. P. Ananthavel, D. H. Waldeck, R. Naaman, Asymmetric scattering of polarized electrons by organized organic films of chiral molecules. *Science* **283**, 814-816 (1999).
4. R. Naaman, Y. Paltiel, D. H. Waldeck, Chiral molecules and the electron spin. *Nat. Rev. Chem.* **3**, 250-260 (2019).
5. C. D. Aiello *et al.*, A chirality-based quantum leap. *ACS Nano* **16**, 4989-5035 (2022).
6. A. Chiesa *et al.*, Chirality-induced spin selectivity: An enabling technology for quantum applications. *Adv. Mater.* 2300472 (2023).
7. S. H. Yang, R. Naaman, Y. Paltiel, S. S. P. Parkin, Chiral spintronics. *Nat. Rev. Phys.* **3**, 328-343 (2021).
8. R. Naaman, Y. Paltiel, D. H. Waldeck, Chiral induced spin selectivity gives a new twist on spin-control in chemistry. *Acc. Chem. Res.* **53**, 2659-2667 (2020).
9. I. Carmeli, K. S. Kumar, O. Heifler, C. Carmeli, R. Naaman, Spin selectivity in electron transfer in photosystem i. *Angew. Chem., Int. Ed.* **53**, 8953-8958 (2014).

10. J. Fransson, Charge and spin dynamics and enantioselectivity in chiral molecules. *J. Phys. Chem. Lett.* **13**, 808-814 (2022).
11. J. Fransson, Charge redistribution and spin polarization driven by correlation induced electron exchange in chiral molecules. *Nano Lett.* **21**, 3026-3032 (2021).
12. J. Fransson, Vibrational origin of exchange splitting and "chiral-induced spin selectivity". *Phys. Rev. B* **102**, 235416 (2020).
13. J. Fransson, Chirality-induced spin selectivity: The role of electron correlations. *J. Phys. Chem. Lett.* **10**, 7126-7132 (2019).
14. S. Naskar, V. Mujica, C. Herrmann, Chiral-induced spin selectivity and non-equilibrium spin accumulation in molecules and interfaces: A first-principles study. *J. Phys. Chem. Lett.* **14**, 694-701 (2023).
15. A. Dianat *et al.*, Role of exchange interactions in the magnetic response and intermolecular recognition of chiral molecules. *Nano Lett.* **20**, 7077-7086 (2020).
16. C.-Z. Wang, V. Mujica, Y.-C. Lai, Spin Fano resonances in chiral molecules: An alternative mechanism for the ciss effect and experimental implications. *Nano Lett.* **21**, 10423-10430 (2021).
17. M. S. Zoellner, S. Varela, E. Medina, V. Mujica, C. Herrmann, Insight into the origin of chiral-induced spin selectivity from a symmetry analysis of electronic transmission. *J. Chem. Theory Comput.* **16**, 2914-2929 (2020).
18. R. Bittl, G. Kothe, Transient EPR of radical pairs in photosynthetic reaction centers: Prediction of quantum beats. *Chem. Phys. Lett.* **177**, 547-553 (1991).
19. G. Kothe, S. Weber, R. Bittl, E. Ohmes, M. C. Thurnauer, J. R. Norris, Transient EPR of light-induced radical pairs in plant photosystem I: Observation of quantum beats. *Chem. Phys. Lett.* **186**, 474-480 (1991).
20. R. Bittl, A. van der Est, A. Kamlowski, W. Lubitz, D. Stehlik, Time-resolved EPR of the radical pair P865⁺Q_a⁻ in bacterial reaction centers. Observation of transient nutations, quantum beats and envelope modulation effects. *Chem. Phys. Lett.* **226**, 349-358 (1994).
21. S. A. Dzuba, P. Gast, A. J. Hoff, ESEEM study of spin-spin interactions in spin-polarized P⁺Q_a⁻ pairs in the photosynthetic purple bacterium *Rhodobacter sphaeroides* R26. *Chem. Phys. Lett.* **236**, 595-602 (1995).
22. M. R. Wasielewski, G. L. Gaines, III, G. P. Wiederrecht, W. A. Svec, M. P. Niemczyk, Biomimetic modeling of photosynthetic reaction center function: Long-lived, spin-polarized radical ion pair formation in chlorophyll-porphyrin-quinone triads. *J. Am. Chem. Soc.* **115**, 10442-10443 (1993).
23. K. Hasharoni, H. Levanon, S. R. Greenfield, D. J. Gosztola, W. A. Svec, M. R. Wasielewski, Mimicry of the radical pair and triplet states in photosynthetic reaction centers with a synthetic model. *J. Am. Chem. Soc.* **117**, 8055-8056 (1995).
24. D. Carbonera *et al.*, EPR investigation of photoinduced radical pair formation and decay to a triplet state in a carotene-porphyrin-fullerene triad. *J. Am. Chem. Soc.* **120**, 4398-4405 (1998).
25. S. M. Harvey, M. R. Wasielewski, Photogenerated spin-correlated radical pairs: From photosynthetic energy transduction to quantum information science. *J. Am. Chem. Soc.* **143**, 15508-15529 (2021).
26. R. Carmieli, T. A. Zeidan, R. F. Kelley, Q. Mi, F. D. Lewis, M. R. Wasielewski, Excited state, charge transfer, and spin dynamics in DNA hairpin conjugates with perylenediimide hairpin linkers. *J. Phys. Chem. A* **113**, 4691-4700 (2009).

27. R. Carmieli *et al.*, Structure and dynamics of photogenerated triplet radical ion pairs in DNA hairpin conjugates with anthraquinone end caps. *J. Am. Chem. Soc.* **134**, 11251-11260 (2012).
28. J. H. Olshansky, M. D. Krzyaniak, R. M. Young, M. R. Wasielewski, Photogenerated spin-entangled qubit (radical) pairs in DNA hairpins: Observation of spin delocalization and coherence. *J. Am. Chem. Soc.* **141**, 2152-2160 (2019).
29. J. H. Olshansky, J. Zhang, M. D. Krzyaniak, E. R. Lorenzo, M. R. Wasielewski, Selectively addressable photogenerated spin qubit pairs in DNA hairpins. *J. Am. Chem. Soc.* **142**, 3346-3350 (2020).
30. E. R. Lorenzo, J. H. Olshansky, D. S. D. Abia, M. D. Krzyaniak, R. M. Young, M. R. Wasielewski, Interaction of photogenerated spin qubit pairs with a third electron spin in DNA hairpins. *J. Am. Chem. Soc.* **143**, 4625-4632 (2021).
31. J. A. Christensen, J. Zhang, J. Zhou, J. N. Nelson, M. R. Wasielewski, Near-infrared excitation of the *peri*-xanthenoxanthene radical cation drives energy-demanding hole transfer reactions. *J. Phys. Chem. C* **122**, 23364-23370 (2018).
32. M.-T. Chen *et al.*, 1,1'-bi(2-naphthol-4,5-dicarboximide)s: Blue emissive axially chiral scaffolds with aggregation-enhanced emission properties. *Org. Chem. Front.* **6**, 3731-3740 (2019).
33. M. C. Thurnauer, J. R. Norris, An electron spin echo phase shift observed in photosynthetic algae : Possible evidence for dynamic radical pair interactions. *Chem. Phys. Lett.* **76**, 557-561 (1980).
34. K. M. Salikhov, Y. E. Kandrashkin, A. K. Salikhov, Peculiarities of free induction and primary spin echo signals for spin-correlated radical pairs. *Appl. Magn. Res.* **3**, 199-216 (1992).
35. J. Tang, M. C. Thurnauer, J. R. Norris, Electron spin echo envelope modulation due to exchange and dipolar interactions in a spin-correlated radical pair. *Chem. Phys. Lett.* **219**, 283-290 (1994).
36. R. Bittl, S. G. Zech, Pulsed EPR study of spin-coupled radical pairs in photosynthetic reaction centers: Measurement of the distance between P700⁺ and A₁⁻ in photosystem I and between P865⁺ and Q_a⁻ in bacterial reaction centers. *J. Phys. Chem. B* **101**, 1429-1436 (1997).
37. S. Santabarbara, I. Kuprov, P. J. Hore, A. Casal, P. Heathcote, M. C. W. Evans, Analysis of the spin-polarized electron spin echo of the [P700⁺A₁⁻] radical pair of photosystem I indicates that both reaction center subunits are competent in electron transfer in cyanobacteria, green algae, and higher plants. *Biochemistry* **45**, 7389-7403 (2006).
38. R. Carmieli, Q. Mi, A. Butler Ricks, E. M. Giacobbe, S. M. Mickley, M. R. Wasielewski, Direct measurement of photoinduced charge separation distances in donor-acceptor systems for artificial photosynthesis using OOP-ESEEM. *J. Am. Chem. Soc.* **131**, 8372-8373 (2009).
39. C. D. Buckley, D. A. Hunter, P. J. Hore, K. A. McLauchlan, Electron spin resonance of spin-correlated radical pairs. *Chem. Phys. Lett.* **135**, 307-312 (1987).
40. G. L. Closs, M. D. E. Forbes, J. R. Norris, Spin-polarized electron-paramagnetic resonance-spectra of radical pairs in micelles - observation of electron spin-spin interactions. *J. Phys. Chem.* **91**, 3592-3599 (1987).
41. A. J. Hoff, P. Gast, S. A. Dzuba, C. R. Timmel, C. E. Fursman, P. J. Hore, The nuts and bolts of distance determination and zero- and double-quantum coherence in photoinduced radical pairs. *Spectrochim. Acta, Part A* **54A**, 2283-2293 (1998).

42. H. Mao, G. J. Pazera, R. M. Young, M. D. Krzyaniak, M. R. Wasielewski, Quantum gate operations on a spectrally addressable photogenerated molecular electron spin-qubit pair. *J. Am. Chem. Soc.* **145**, 6585-6593 (2023).
43. Y. Wu, M. D. Krzyaniak, J. F. Stoddart, M. R. Wasielewski, Spin frustration in the triradical trianion of a naphthalenediimide molecular triangle. *J. Am. Chem. Soc.* **139**, 2948-2951 (2017).
44. T. P. Fay, D. T. Limmer, Origin of chirality induced spin selectivity in photoinduced electron transfer. *Nano Lett.* **21**, 6696-6702 (2021).
45. T. P. Fay, Chirality-induced spin coherence in electron transfer reactions. *J. Phys. Chem. Lett.* **12**, 1407-1412 (2021).
46. J. Luo, P. J. Hore, Chiral-induced spin selectivity in the formation and recombination of radical pairs: Cryptochrome magnetoreception and EPR detection. *New J. Phys.* **23**, 043032 (2021).
47. A. Chiesa *et al.*, Assessing the nature of chiral-induced spin selectivity by magnetic resonance. *J. Phys. Chem. Lett.* **12**, 6341-6347 (2021).
48. D. Amsallem, A. Kumar, R. Naaman, O. Gidron, Spin polarization through axially chiral linkers: Length dependence and correlation with the dissymmetry factor. *Chirality* **35**, 562-568 (2023).
49. H. J. Eckvahl *et al.*, Direct observation of chirality-induced spin selectivity in electron donor-acceptor molecules. Dryad: doi.org/10.5061/dryad.fbg79cp1r (2023).
50. A. Sciutto *et al.*, Customizing photoredox properties of PXX-based dyes through energy level rigid shifts of frontier molecular orbitals. *Chem. - Eur. J.* **24**, 4382-4389 (2018).
51. J. L. Sessler *et al.*, A rigid chlorin-naphthalene diimide conjugate. A possible new noncovalent electron transfer model system. *J. Org. Chem.* **63**, 7370-7374 (1998).
52. R. M. Young *et al.*, Ultrafast conformational dynamics of electron transfer in exbox⁴⁺-perylene. *J. Phys. Chem. A* **117**, 12438-12448 (2013).
53. D. Gosztola, M. P. Niemczyk, W. Svec, A. S. Lukas, M. R. Wasielewski, Excited doublet states of electrochemically generated aromatic imide and diimide radical anions. *J. Phys. Chem. A* **104**, 6545-6551 (2000).
54. S. Stoll, A. Schweiger, Easyspin, a comprehensive software package for spectral simulation and analysis in EPR. *J. Magn. Reson.* **178**, 42-55 (2006).
55. C. E. Tait, M. D. Krzyaniak, S. Stoll, Computational tools for the simulation and analysis of spin-polarized EPR spectra. *J. Magn. Reson.* **349**, 107410 (2023).
56. Y. Shao *et al.*, Advances in molecular quantum chemistry contained in the Q-Chem 4 program package. *Mol. Phys.* **113**, 184-215 (2015).
57. P. J. Hore, in *Advanced EPR in biology and biochemistry*, A. J. Hoff, Ed. (Elsevier, Amsterdam, 1989), pp. 405-440.
58. A. Weller, Photoinduced electron transfer in solution: Exciplex and radical ion pair formation free enthalpies and their solvent dependence. *Z. Phys. Chem.* **133**, 93-99 (1982).
59. H. Mao, R. M. Young, M. D. Krzyaniak, M. R. Wasielewski, Controlling the dynamics of three electron spin qubits in a donor-acceptor-radical molecule using dielectric environment changes. *J. Phys. Chem. Lett.* **12**, 2213-2218 (2021).
60. G. L. Closs, J. R. Miller, Intramolecular long-distance electron transfer in organic molecules. *Science* **240**, 440-447 (1988).

Acknowledgments:

Funding:

This work was supported by the National Science Foundation under award no. CHE-2154627 (M.R.W., synthesis, transient optical and EPR measurements).

Research supported as part of the Center for Molecular Quantum Transduction, an Energy Frontier Research Center funded by the U.S. Department of Energy (DOE), Office of Science, Basic Energy Sciences (BES), under award DE-SC0021314 (M.D.K., EPR data analysis).

This work was supported by the ERC-Synergy project CASTLE (project no. 101071533) funded by the Horizon Europe Program and the Fondazione Cariparma (S.C., calculations).

¹H nuclear magnetic resonance (NMR) spectroscopy, and mass spectrometry are conducted in IMSERC facilities at Northwestern University, which have received support from the Soft and Hybrid Nanotechnology Experimental (SHyNE) Resource (NSF ECCS-2025633), NSF CHE-1048773, Northwestern University, the State of Illinois, and the International Institute for Nanotechnology (IIN).

Author contributions:

Conceptualization: MRW

Methodology: HJE, NAT, JMB, MDK, AC, SC, RMY, MRW

Investigation: HJE, NAT, JMB, MDK, AC, SC, RMY, MRW

Visualization: HJE, NAT, AC, RMY, MRW

Funding acquisition: MRW, SC

Project administration: MRW

Supervision: MRW, MDK, SC

Writing – original draft: MRW, MDK, HJE, NAT, SC, AC

Writing – review & editing: MRW, MDK, HJE, NAT, SC, AC

Competing interests:

Authors declare that they have no competing interests.

Data and materials availability:

All data are available in the main text, the supplementary materials, and in Dryad(49).

Supplementary Materials

Materials and Methods

Supplementary Text

Figs. S1 to S12

Tables S1 to S7

References (50-60)

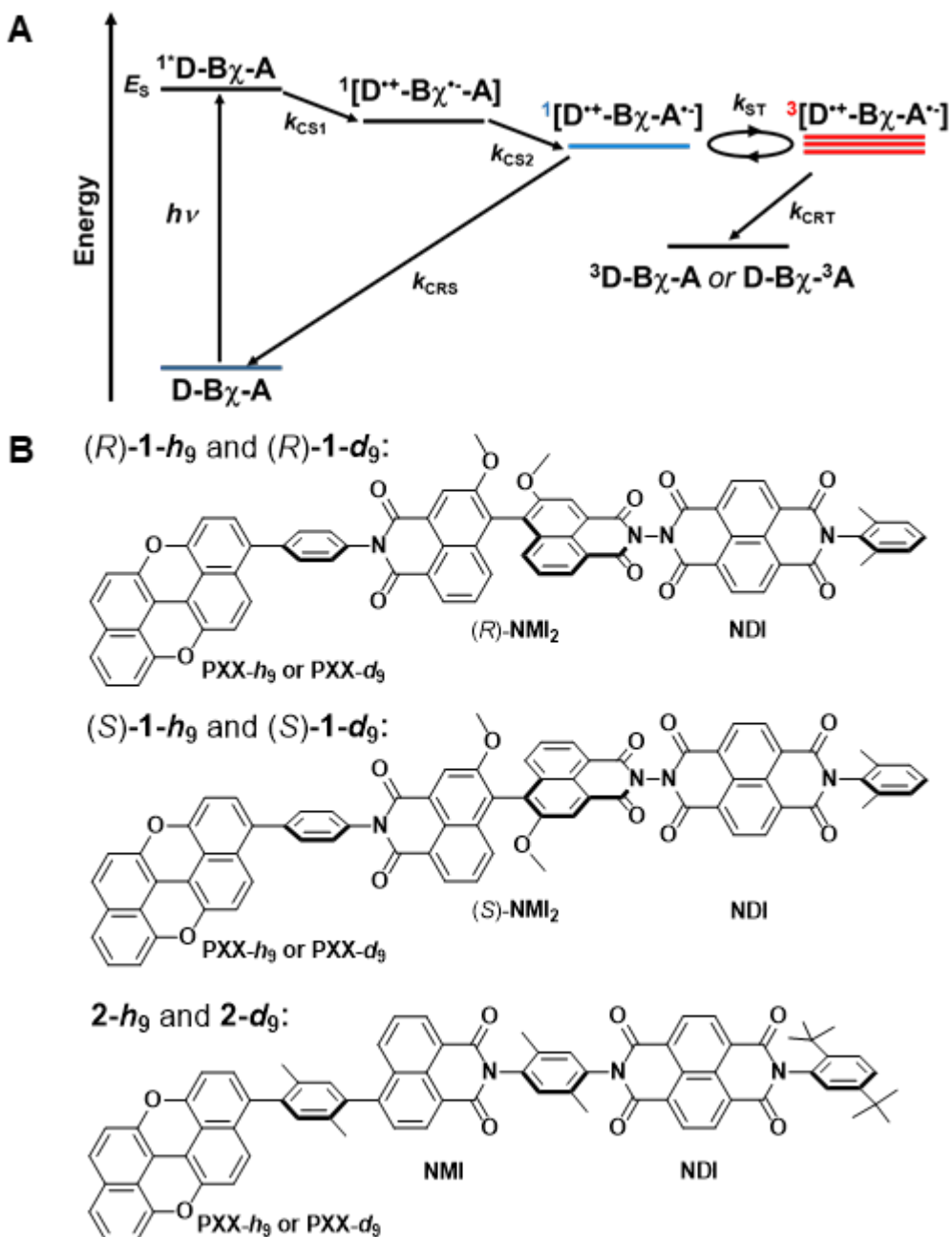


Fig. 1. Electron transfer pathways and molecular structures. (A) Electron transfer and intersystem crossing pathways in a D-B χ -A system with no applied magnetic field, where k_{CS1} and k_{CS2} are the charge separation rate constants, k_{ST} is singlet-triplet mixing rate constant, and k_{CRS} and k_{CRT} are the charge recombination rates via the singlet and triplet channels, respectively. (B) Structures of chiral (*R*)-**1** and (*S*)-**1** and achiral **2**. The steric constraints imposed by linking the two NMI groups in (*R*)-**1** and (*S*)-**1** result in stable enantiomers having axial chirality.

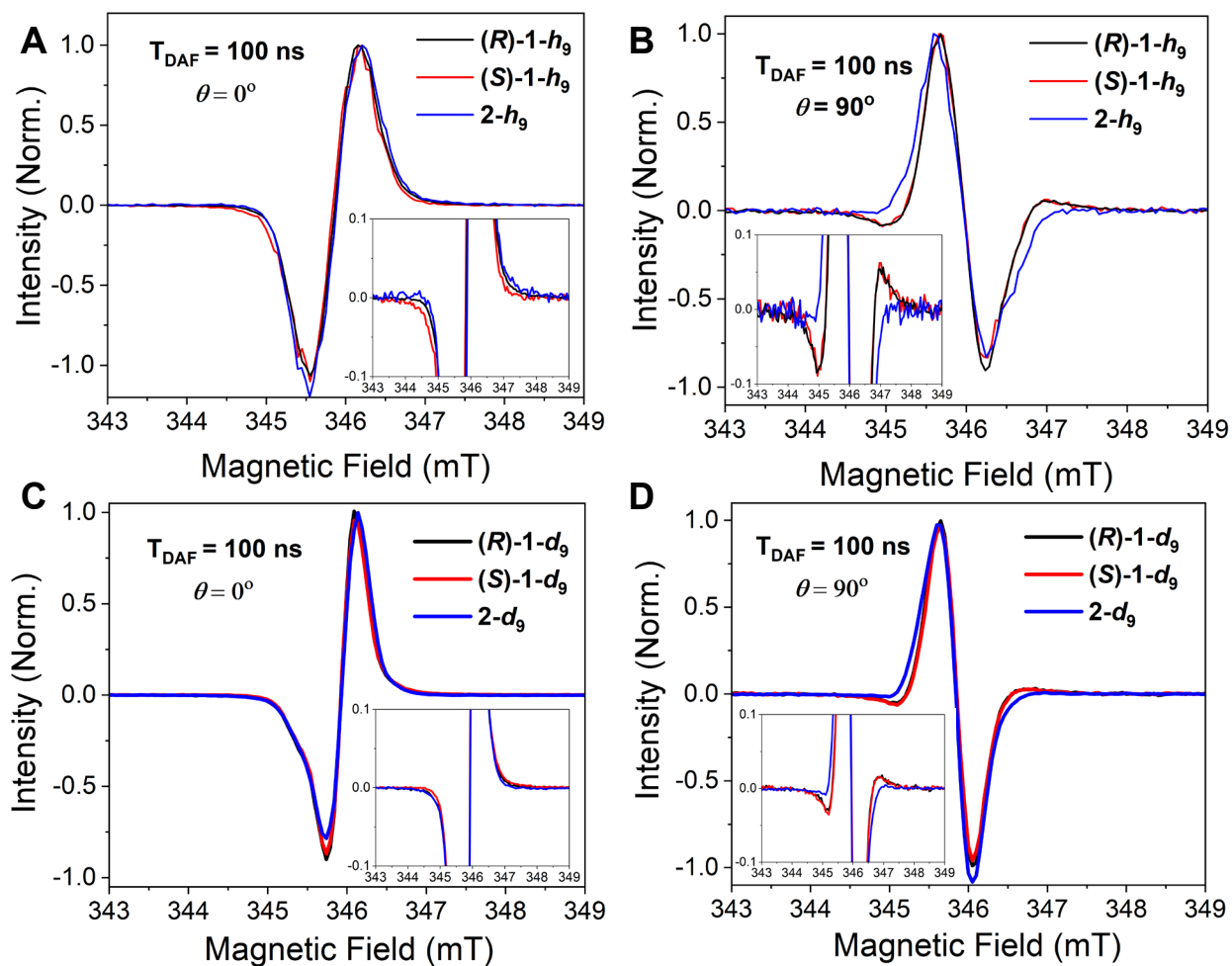


Fig. 2. TREPR spectra. TREPR spectra of (R)-1- h_9 , (S)-1- h_9 , and 2- h_9 (A, B) and (R)-1- d_9 , (S)-1- d_9 , and 2- d_9 (C, D) oriented in the nematic liquid crystal 5CB at 85 K and 100 ns after a 450 nm, 7 ns laser pulse with the long axis of each molecule (A, C) 0° and (B, D) 90° relative to the applied magnetic field direction. Insets: the spectra are shown with their intensities expanded to highlight features characteristic of CISS.

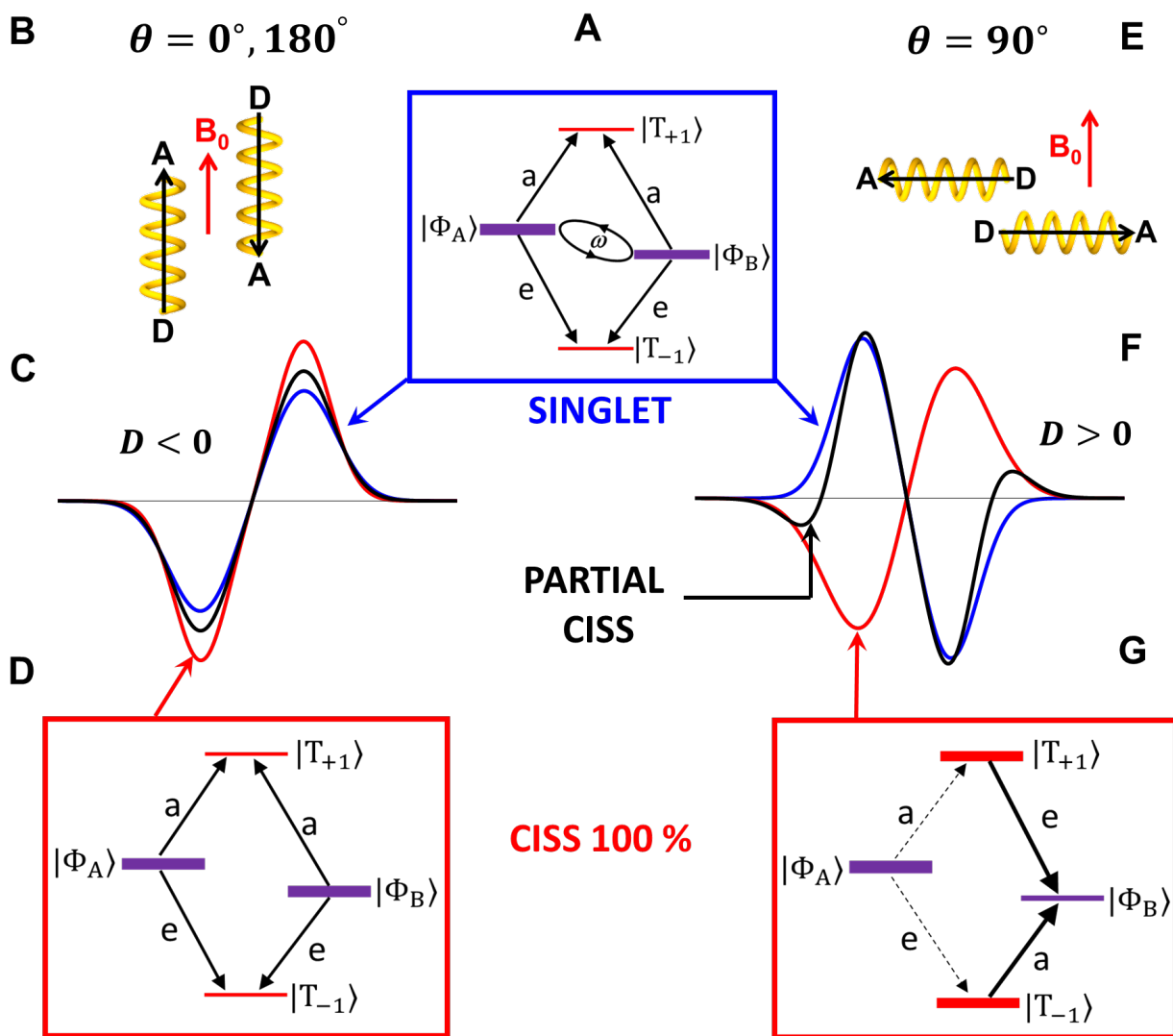


Fig. 3. The CISS effect on the spin states of SCRPs. (A) SCRPs spin states in the absence of CISS and in the presence of a static magnetic field B_0 that is much greater than J , D , and the hyperfine interactions in both radicals for a singlet precursor. The enhanced absorptive (a) and emissive (e) microwave-induced EPR transitions are indicated. (B) Schematic of chiral molecules aligned parallel to B_0 . (C) TREPR spectra with $\theta = 0^\circ$ expected for an achiral SCR (blue trace) and for a chiral SCR with an initial state having 100% CISS contribution (red trace) or a partial CISS contribution (black trace). (D) SCRPs spin states for $\theta = 0^\circ$ where the initial state has a 100% CISS contribution. (E) Schematic of chiral molecules aligned perpendicular to B_0 . (F) TREPR spectra with $\theta = 90^\circ$ expected for an achiral SCR (blue trace) and for a chiral SCR with an initial state having 100% CISS contribution (red trace) or a partial CISS contribution (black trace, rescaled). (G) SCRPs spin states for $\theta = 90^\circ$ where the initial state has a 100% CISS contribution. The width of the energy levels in (A), (D), and (G) indicates the population of the initial state, while the relative arrow thicknesses in the boxes depict the transition probabilities.

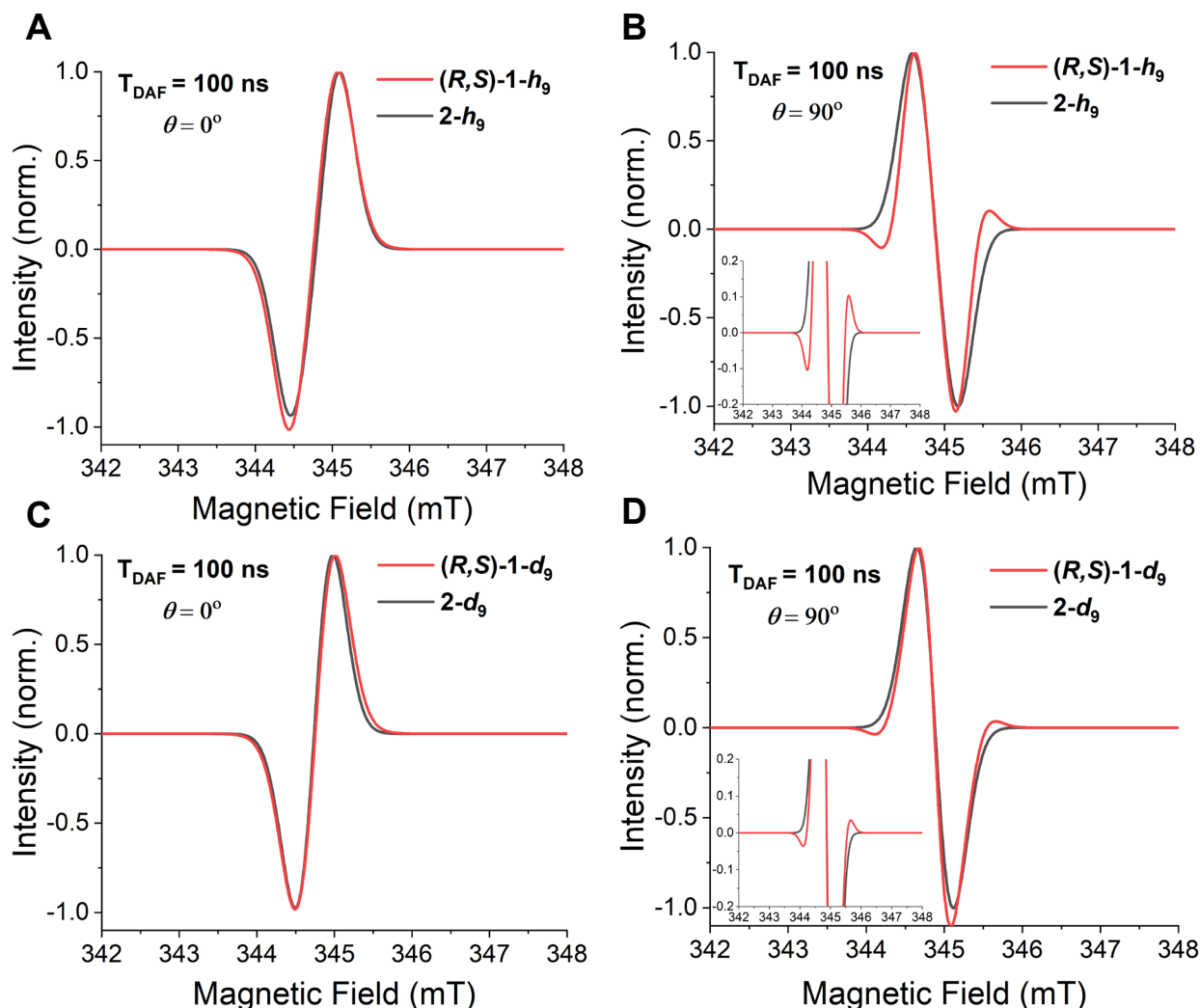


Fig. 4. Simulations of the TREPR spectra with a minimal model of the SCRCP. The model places one hydrogen nuclear spin- $\frac{1}{2}$ on both PXX^+ and NDI^- (**A**, **B**) or only on NDI^- (**C**, **D**). The nuclear spins are coupled to each radical with isotropic hyperfine couplings $a_{\text{NDI}} = 6.3$ MHz and $a_{\text{PXX}} = 10$ MHz. Insets: the simulations are shown with their intensities expanded to highlight features characteristic of CISS. The complete list of simulation parameters is given in table S7.



Supplementary Materials for
**Direct Observation of Chirality-Induced Spin Selectivity in
Electron Donor-Acceptor Molecules**

Hannah J. Eckvahl,^{1†} Nikolai A. Tcyrulnikov,^{1†} Alessandro Chiesa,^{2†} Jillian M. Bradley,¹ Ryan M. Young,¹ Stefano Carretta,^{2*} Matthew D. Krzyaniak,^{1*} and Michael R. Wasielewski^{1*}

¹Department of Chemistry, Center for Molecular Quantum Transduction, and Paula M. Trienens Institute for Sustainability and Energy, Northwestern University, Evanston, IL 60208-3113 USA.

²Università di Parma, Dipartimento di Scienze Matematiche, Fisiche e Informatiche, Parma, I-43124, Italy.

*Corresponding authors. Email: m-wasielewski@northwestern.edu; mdkrzyaniak@northwestern.edu; stefano.carretta@unipr.it

†These authors contributed equally to this work

The PDF file includes:

Materials and Methods
Supplementary Text
Figs. S1 to S12
Tables S1 to S7
References (50-60)

Materials and Methods

Synthesis

The synthetic schemes and structures of the intermediates and final structures are illustrated in Figs. S1-S2. All commercially available materials were used without further purification unless otherwise noted. Characterization of synthesized compounds was performed at Integrated Molecular Structure Education and Research Center (IMSERC) at Northwestern University. Proton and carbon NMR spectra were recorded on a Bruker Avance III 500 MHz system equipped with DCH CryoProbe. Shifts are reported in parts-per-million (ppm) relative to TMS. High Resolution Mass Spectra (HRMS) were obtained with an Agilent LCTOF 6200 series mass spectrometer using electrospray ionization (ESI), APCI, and APPI. CD spectra were obtained with Jasco J-815 CD Instrument Keck Biophysics Facility at Northwestern University.

NIA-xyl. In a 250 mL two-neck round bottom flask equipped with a condenser and a dropping funnel, 1,4,5,8-naphthalenetetracarboxylic dianhydride (3.0 g, 11.2 mmol, regenerated prior to use by refluxing overnight in acetic anhydride followed by the removal of the acetic anhydride under reduced pressure) was suspended in 40 mL of dry *N,N*-dimethylformamide. The mixture was heated to reflux under an inert atmosphere and stirred for two hours to ensure the dissolution of the 1,4,5,8-naphthalenetetracarboxylic dianhydride. To this vigorously stirred solution, 2,6-xylidine (677 mg, 5.6 mmol) in 50 ml of dry *N,N*-dimethylformamide was added via a dropping funnel over several hours. The reaction mixture was refluxed overnight under an inert atmosphere, cooled down to room temperature, and the solvent removed under reduced pressure. The crude material was purified by silica gel chromatography (100 % dichloromethane), affording **NIA-xyl** as a brown powder (800 mg, 2.15 mmol, 38 %). ¹H NMR (500 MHz, CD₂Cl₂, δ): 8.76-8.80 (m, 4H), 7.27 (m, 1H), 7.19 (m, 2H), 2.05 (m, 6H). ¹³C NMR (126 MHz, CDCl₃, δ): 161.43, 160.90, 158.25, 135.00, 134.92, 132.76, 132.47, 132.38, 130.81, 130.60, 128.42, 128.30, 128.26, 127.85,

127.80, 127.04, 126.85, 126.76, 126.14, 122.36, 16.80. ESI-HRMS (m/z): calculated for $C_{23}H_9N_5O$ $[M]^+$: 371.0813, found: 371.0803.

NH₂-NDI-xyI. In a 25 mL round bottom flask equipped with a condenser, **NIA-xyI** (300 mg, 0.81 mmol) was suspended in 10 mL of dry *N,N*-dimethylformamide. The mixture was heated to reflux and stirred for one hour. Hydrazine monohydrate (0.5 mL) was added, and the reaction mixture was refluxed for 3 hours. The reaction mixture was cooled to room temperature and the solvent was removed under reduced pressure. The crude material was dissolved in dichloromethane and washed twice with brine. The organic layer was dried over sodium sulfate, filtered, and concentrated under reduced pressure. The crude material was purified by silica gel chromatography (20 % ethyl acetate in dichloromethane), affording **NH₂-NDI-xyI** as a yellow solid (270 mg, 0.70 mmol, 87 %). ¹H NMR (500 MHz, CD₂Cl₂, δ): 8.71-8.76 (m, 4H), 7.26 (m, 1H), 7.18 (d, *J* = 7.7 Hz, 2H), 5.52 (s, 2H), 2.04 (s, 6H). ¹³C NMR (126 MHz, CD₂Cl₂, δ): 161.32, 158.81, 135.00, 132.71, 130.58, 130.34, 128.28, 127.78, 126.64, 126.13, 125.49, 124.83, 16.82. ESI-HRMS (m/z): calculated for $C_{22}H_{15}N_3O_4$ $[M+H]^+$: 386.1135, found: 386.1152.

NMA-NMI-NDI-xyI. In a 25 mL two-neck round bottom flask equipped with a condenser and a dropping funnel, 5,5'-dimethoxy-1H,1'H,3H,3'H-[6,6'-bibenzo[de]isochromene]-1,1',3,3'-tetraone(50) (327 mg, 0.72 mmol) was suspended in 10 mL of dry *N,N*-dimethylformamide and the mixture was refluxed for one hour under inert atmosphere. To this, **NH₂-NDI-xyI** (250 mg, 0.65 mmol) dissolved in 50 mL of dry *N,N*-dimethylformamide was added via a dropping funnel over several hours, and the reaction mixture was further refluxed overnight under an inert atmosphere. The reaction mixture was cooled to room temperature and the solvent was removed under reduced pressure. Due to purification difficulties and the tendency of the product to undergo hydrolysis of the anhydride moiety, the crude material was passed through a silica gel pad (10 % ethyl acetate in dichloromethane) and used without further purification right away. A small

fraction of the crude was purified using preparatory TLC for characterization. ^1H NMR (500 MHz, CD_2Cl_2 , δ): 8.84 (m, 4H), 8.55 (s, 1H), 8.47-8.51 (m, 2H), 8.43 (d, $J = 6.8$ Hz, 1H), 7.51-7.57 (m, 2H), 7.28 (m, 1H), 7.21 (d, $J = 7.6$ Hz, 2H), 3.87 (s, 3H), 3.84 (s, 3H), 2.08 (s, 6H). ^{13}C NMR (126 MHz, CD_2Cl_2 , δ): 162.00, 160.53, 160.44, 159.92, 159.86, 156.06, 155.87, 133.44, 132.61, 132.48, 132.22, 132.08, 132.05, 131.46, 131.43, 131.32, 130.47, 129.11, 128.58, 128.29, 128.00, 127.81, 127.56, 127.48, 126.41, 126.10, 125.93, 125.46, 124.25, 123.76, 122.09, 120.58, 119.01, 118.72, 117.95, 29.68, 17.59. APCI-HRMS (m/z): calculated for $\text{C}_{48}\text{H}_{27}\text{N}_3\text{O}_{11}$ $[\text{M}]^+$: 821.1651, found: 821.1627.

Br-Ph-(NMI)₂-NDI-xyl. In a 50 mL round bottom flask equipped with a condenser, **NMA-NMI-NDI-xyl** (210 mg, crude), 4-bromoaniline (132 mg, 0.77 mmol), and zinc (II) acetate dihydrate (15 mg) were dissolved in 20 mL of dry *N,N*-dimethylformamide and the mixture was refluxed overnight under an inert atmosphere. The reaction mixture was cooled to room temperature and the solvent was removed under reduced pressure. The crude material was purified by silica gel chromatography (gradient from 100 % dichloromethane to 5 % ethyl acetate in dichloromethane), affording **Br-Ph-(NMI)₂-NDI-xyl** as a brown solid (40 mg, 0.30 mmol). ^1H NMR (500 MHz, CD_2Cl_2 , δ): 8.80-8.90 (m, 4H), 8.56 (s, 1H), 8.50 (m, 2H), 8.43 (dd, $J_1 = 7.0$ Hz, $J_2 = 1.1$ Hz, 1H), 7.66 (d, $J = 8.6$ Hz, 2H), 7.49-7.58 (m, 3H), 7.45 (dd, $J_1 = 8.6$ Hz, $J_2 = 1.1$ Hz, 1H), 7.29 (m, 1H), 7.18-7.23 (m, 4H), 3.86 (m, 6H), 2.08 (s, 6H). ^{13}C NMR (126 MHz, CD_2Cl_2 , δ): 163.20, 163.01, 161.25, 159.99, 159.96, 159.18, 159.11, 155.13, 155.07, 135.02, 135.01, 134.05, 132.66, 131.99, 131.72, 131.64, 131.57, 131.33, 131.30, 130.72, 130.70, 130.49, 129.87, 129.70, 128.69, 128.36, 127.83, 127.19, 127.13, 127.03, 126.75, 126.70, 125.64, 125.44, 123.90, 123.80, 123.48, 123.34, 122.74, 122.08, 121.75, 121.24, 117.19, 116.37, 28.93, 16.85. ESI-HRMS (m/z): calculated for $\text{C}_{54}\text{H}_{31}\text{BrN}_4\text{O}_{10}\text{Na}$ $[\text{M}+\text{Na}]^+$: 999.1109, found: 999.1125.

(R,S)-1-d9. In a 25 mL round bottom two-neck flask equipped with a condenser and a septum were combined **Br-Ph-(NMI)₂-NDI-xyl** (20 mg, 0.02 mmol), PXX-*d*₉-Bpin (Fig. S2) (17 mg, 0.04 mmol), [1,1'-bis(diphenylphosphino)ferrocene]dichloropalladium(II) (3 mg, 0.004 mmol), and potassium carbonate (20 mg). The flask was evacuated and filled with nitrogen three times. To this mixture, 10 mL of a degassed mixture of toluene, ethanol, and water (2/1/1 vol. ratio) was added through the septum. The reaction mixture was heated at 110 °C overnight under an inert atmosphere. The reaction mixture was cooled to room temperature, dissolved in dichloromethane, and washed twice with brine. The organic layer was dried over sodium sulfate, filtered, and concentrated under reduced pressure. The crude material was purified by silica gel chromatography (gradient from 100 % dichloromethane to 5 % ethyl acetate in dichloromethane), affording **(R,S)-1-d9** as a yellow solid (17 mg, 0.014 mmol, 72 %). ¹H NMR (500 MHz, CD₂Cl₂, δ): 8.81-8.88 (m, 4H), 8.58 (s, 1H), 8.55 (s, 1H), 8.51 (dd, J₁ = 6.5 Hz, J₂ = 1.5 Hz, 1H), 8.47 (dd, J₁ = 7.0 Hz, J₂ = 1.0 Hz, 1H), 7.62 (d, J = 8.4 Hz, 2H), 7.52-7.60 (m, 3H), 7.47 (dd, J₁ = 8.5 Hz, J₂ = 1.0 Hz, 1H), 7.41 (d, J = 8.2 Hz, 2H), 7.29 (m, 1H), 7.21 (d, J = 7.7 Hz, 2H), 3.89 (s, 3H), 3.87 (s, 3H), 2.09 (s, 6H). ¹³C NMR (126 MHz, CD₂Cl₂, δ): 163.48, 163.29, 161.26, 160.02, 159.98, 159.19, 159.12, 155.16, 155.09, 151.74, 151.60, 143.78, 143.36, 139.24, 135.03, 134.10, 132.66, 132.03, 131.65, 131.34, 131.31, 130.72, 130.47, 130.38, 129.72, 129.41, 128.65, 128.35, 128.25, 127.83, 127.20, 127.14, 127.03, 126.76, 125.65, 125.55, 124.03, 123.77, 123.50, 123.40, 122.73, 122.30, 121.25, 121.09, 120.70, 117.22, 116.36, 110.96, 110.56, 28.93, 16.86. APPI-HRMS (*m/z*): calculated for C₇₄H₃₁D₉N₄O₁₂ [M]⁺: 1185.3208, found: 1185.3225.

(R,S)-1-h9. Using a procedure described for the synthesis of **(R,S)-1-d9**, **(R,S)-1-h9** was obtained from 20 mg (0.02 mmol) of **D** and 18 mg of PXX-Bpin(3I) as a yellow solid (16 mg, 66 %). ¹H NMR (500 MHz, CD₂Cl₂, δ): 8.81-8.88 (m, 4H), 8.58 (s, 1H), 8.55 (s, 1H), 8.51 (dd, J₁ = 6.6 Hz, J₂ = 1.4 Hz, 1H), 8.47 (dd, J₁ = 7.0 Hz, J₂ = 0.7 Hz, 1H), 7.63 (d, J = 8.2 Hz, 2H), 7.50-

7.59 (m, 4H), 7.46 (dd, $J_1 = 8.2$ Hz, $J_2 = 0.8$ Hz, 1H), 7.41 (d, $J = 8.2$ Hz, 2H), 7.26-7.33 (m, 2H), 7.21 (d, $J = 7.6$ Hz, 2H), 7.16 (d, $J = 7.8$ Hz, 1H), 7.05-7.10 (m, 2H), 6.92 (dd, $J_1 = 9.1$ Hz, $J_2 = 3.7$ Hz, 2H), 6.74 (d, $J = 7.8$ Hz, 1H), 6.62 (dd, $J_1 = 5.6$ Hz, $J_2 = 1.8$ Hz, 1H), 3.89 (s, 3H), 3.87 (s, 3H), 2.09 (s, 6H). ^{13}C NMR (126 MHz, CD_2Cl_2 , δ): 163.47, 163.28, 161.26, 160.02, 159.99, 159.19, 159.13, 155.22, 155.15, 151.83, 151.68, 143.87, 143.46, 139.29, 135.05, 135.03, 134.15, 132.70, 132.08, 131.70, 131.62, 131.51, 131.33, 131.30, 130.71, 130.37, 129.71, 129.42, 128.65, 128.50, 128.36, 128.27, 127.83, 127.58, 127.20, 127.13, 127.06, 126.81, 126.80, 126.74, 126.48, 125.84, 125.69, 125.62, 124.38, 124.09, 123.84, 123.55, 123.45, 122.78, 122.37, 121.31, 121.12, 120.75, 119.47, 117.28, 116.81, 116.55, 116.43, 111.00, 110.61, 108.07, 107.94, 28.93, 16.84. ESI-HRMS (m/z): calculated for $\text{C}_{74}\text{H}_{41}\text{N}_4\text{O}_{12}$ [$\text{M}+\text{H}$] $^+$: 1177.2715, found: 1177.2707.

PXX-*d*₉-Br. Under a nitrogen atmosphere, **PXX-*d*₁₀** (42) (1 eq, 0.34 mmol, 100 mg) and *N*-bromosuccinimide (1 eq, 0.34 mmol, 60.9 mg) were suspended in dry dimethylformamide (6.5 mL). The mixture was sparged with nitrogen for 15 minutes, then stirred at room temperature for 16 hr. The mixture was poured into water (60 mL) and vacuum filtered. The yellow solid was washed three times with water (20 mL), then dried in a vacuum oven overnight to yield **PXX-*d*₉-Br** as a dull yellow solid (104 mg). The product was used without further purification.

PXX-*d*₉-Bpin. Under a nitrogen atmosphere, **PXX-*d*₉-Br** (1 eq, 0.28 mmol 103 mg), bis(pinacolato)diboron (3 eq, 0.83 mmol, 212 mg), potassium acetate (6 eq, 1.67 mmol, 164 mg), and [1,1'-bis(diphenylphosphino)ferrocene]dichloropalladium(II) (0.05 eq, 0.014 mmol, 10.2 mg) were dissolved in dioxanes (15 mL, stored in an inert atmosphere over molecular sieves). The mixture was sparged with nitrogen for 15 minutes, then stirred at reflux 12 hr. After cooling to room temperature, the solvent was removed under reduced pressure. The product was purified with flash chromatography (50/50 hexanes/dichloromethane mobile phase), yielding **PXX-*d*₉-Bpin** as a fluorescent yellow solid (50 mg, 43%). ^1H NMR (500 MHz, CDCl_3 , δ): 1.37. ^{13}C NMR (126

MHz, CDCl₃, δ): 155.43, 152.63, 144.22, 143.75, 135.20, 131.25, 121.47, 121.35, 111.91, 111.28, 83.51, 24.98. ESI-HRMS (*m/z*): calculated for C₂₆H₁₂D₉BO₄ [M]⁺: 417.2098, found: 417.2120.

PXX-*d*₉-xy-Br. Under a nitrogen atmosphere, **PXX-*d*₉-Bpin** (1 eq, 0.083 mmol 34.2 mg), 2,5-dibromo-*p*-xylene (20 eq, 1.64 mmol, 433 mg), potassium carbonate (4 eq, 0.32 mmol, 45.3 mg), and tetrakis(triphenylphosphine)palladium(0) (0.05 eq, 0.004 mmol, 4.8 mg) were dissolved in dioxanes (10 mL, distilled, then stored in an inert atmosphere over molecular sieves) and water (1 mL). The mixture was sparged with nitrogen for 15 minutes, then stirred at reflux 12 hr. After cooling to room temperature, the solvent was removed under reduced pressure. The product was purified with flash chromatography (90/10 hexanes/dichloromethane mobile phase), yielding **PXX-*d*₉-xy-Br** as a fluorescent yellow solid (31 mg, 80%). ¹H NMR (500 MHz, CDCl₃, δ): 7.47 (s, 1H), 7.05 (s, 1H), 2.38 (s, 3H), 2.01 (s, 3H). ¹³C NMR (126 MHz, CDCl₃, δ): 152.58, 152.10, 144.44, 144.18, 138.27, 136.23, 135.15, 133.55, 132.52, 131.38, 131.18, 129.48, 123.83, 121.56, 121.52, 111.76, 111.39, 22.31, 19.14. ESI-HRMS (*m/z*): calculated for C₂₈H₈D₉BrO₂ [M]⁺: 473.0977, found: 473.0990.

PXX-*d*₉-xy-Bpin. Under a nitrogen atmosphere, **PXX-*d*₉-xy-Br** (1 eq, 0.046 mmol 21.5 mg), bis(pinacolato)diboron (2 eq, 0.092 mmol, 23.4 mg), potassium acetate (4 eq, 0.18 mmol, 18 mg), and [1,1'-bis(diphenylphosphino)ferrocene]dichloropalladium(II) (0.05 eq, 0.0023 mmol, 1.7 mg) were dissolved in dioxanes (5 mL, distilled, then stored in an inert atmosphere over molecular sieves). The mixture was sparged with nitrogen for 15 minutes, then stirred at reflux 12 hr. After cooling to room temperature, the solvent was removed under reduced pressure. The product was purified with flash chromatography (70/30 hexanes/dichloromethane mobile phase), yielding **PXX-*d*₉-xy-Bpin** as a fluorescent yellow solid (18 mg, 75%). ¹H NMR (500 MHz, CDCl₃, δ): 7.69 (s, 1H), 7.00 (s, 1H), 2.52 (s, 3H), 2.03 (s, 3H), 1.36 (s, 12H). ¹³C NMR (126 MHz, CDCl₃, δ): 152.64, 151.90, 144.37, 144.21, 142.28, 141.58, 137.55, 132.94, 132.60, 131.78, 131.17, 129.48,

121.60, 121.46, 111.63, 111.50, 88.26, 83.47, 29.71, 24.93, 24.92, 21.66, 19.11. ESI-HRMS (m/z): calculated for $C_{34}H_{20}D_9BO_4 [M]^+$: 521.2724, found: 521.2755.

Br-NMI-NDI-dtbp. **NIA-dtbp** and **Br-NMI-NH₂** were synthesized as previously reported.^(38, 51) Under a nitrogen atmosphere, Br-NMI-NH₂ (1 eq, 0.25 mmol, 100 mg) and NIA-dtbp (1.5 eq, 0.38 mmol, 173 mg) were dissolved in ethanol (5 mL, 100%). The mixture was sparged with nitrogen for 15 minutes, then stirred at reflux 12 h (overnight). The precipitate was isolated by vacuum filtration while the mixture was still hot, yielding **Br-NMI-NDI-dtbp** as a white powder (142 mg, 67 %). ¹H NMR (500 MHz, CDCl₃, δ): 8.89-8.84 (m, 4H), 8.37 (dd, $J_1 = 7.3$ Hz, $J_2 = 1.2$ Hz, 1H), 8.66 (dd, $J_1 = 8.6$ Hz, $J_2 = 1.2$ Hz, 1H), 8.49 (d, $J = 7.8$ Hz, 1H), 8.11 (d, $J = 7.9$ Hz, 1H), 7.91 (dd, $J_1 = 8.6$ Hz, $J_2 = 7.2$ Hz, 1H), 7.60 (d, $J = 8.7$ Hz, 1H), 7.48 (dd, $J_1 = 8.6$ Hz, $J_2 = 2.3$ Hz, 1H), 7.28-7.21 (m, 2H), 7.00 (dd, $J_1 = 7.3$ Hz, $J_2 = 2.2$ Hz, 1H), 2.21-2.26 (m, 6H), 1.33-1.30 (m, 9H), 1.27 (s, 9H). ¹³C NMR (126 MHz, CDCl₃, δ): 163.84, 163.24, 163.21, 162.42, 150.39, 143.68, 143.66, 135.16, 134.84, 134.79, 134.27, 133.81, 132.59, 131.99, 131.97, 131.75, 131.54, 131.29, 131.23, 130.97, 130.90, 130.88, 129.52, 129.03, 129.01, 128.27, 127.49, 127.46, 127.43, 127.32, 127.29, 127.16, 126.93, 126.73, 123.12, 122.23, 35.57, 34.28, 31.74, 31.19, 17.40. APPI-HRMS (m/z): calculated for $C_{48}H_{38}BrN_3O_6Na [M+Na]^+$: 854.1842, found: 854.1827.

2-d₉. Under a nitrogen atmosphere, **PXX-d₉-xy-Bpin** (1.22 eq, 0.029 mmol 15 mg), **Br-NMI-NDI-dtbp** (1 eq, 0.024 mmol, 19.7 mg), potassium carbonate (2.5 eq, 0.059 mmol, 8.2 mg), and [1,1'-bis(diphenylphosphino)ferrocene]dichloropalladium(II) (0.1 eq, 0.0023 mmol, 1.7 mg) were dissolved in dioxanes (5 mL, distilled, then stored in an inert atmosphere over molecular sieves) and water (0.5 mL, distilled). The mixture was sparged with nitrogen for 15 minutes, then stirred at reflux 12 h (overnight). After cooling to room temperature, the solvent was removed under reduced pressure. The product was purified with flash chromatography (dichloromethane eluent),

yielding **2-d9** as a yellow solid (14 mg, 42%). ¹H NMR (500 MHz, CDCl₃, δ): 8.90-8.81 (m, 4H), 8.78-8.69 (m, 2H), 8.08 (t, J = 8.0 Hz, 1H), 7.80 (t, J = 7.8 Hz, 1H), 7.62 (t, J = 8.4 Hz, 1H), 7.60 (d, J = 8.7 Hz, 1H), 7.48 (dd, J₁ = 8.6 Hz, J₂ = 2.3 Hz, 1H), 7.31 (d, J = 3.0 Hz, 1H), 7.24-7.19 (m, 2H), 7.02 (dd, J₁ = 13.6 Hz, J₂ = 2.2 Hz, 1H), 2.27-2.18 (m, 6H), 2.13 (s, 3H), 2.07 (s, 3H), 1.34-1.31 (m, 9H), 1.28 (s, 9H). ¹³C NMR (126 MHz, CDCl₃, δ): 163.92, 163.86, 163.73, 162.39, 152.60, 152.14, 150.40, 147.28, 147.27, 147.23, 147.21, 144.48, 144.25, 144.23, 143.75, 143.73, 139.53, 139.49, 137.54, 137.48, 135.58, 135.24, 135.22, 134.73, 134.67, 134.45, 134.44, 134.40, 134.39, 134.20, 133.64, 133.62, 133.58, 133.57, 133.25, 133.18, 132.24, 132.08, 132.06, 132.01, 131.96, 131.71, 131.69, 131.61, 131.59, 131.50, 131.48, 131.35, 131.34, 131.32, 131.22, 130.93, 130.87, 130.82, 129.67, 129.59, 129.03, 129.00, 128.97, 128.12, 128.07, 127.57, 127.54, 127.50, 127.45, 127.35, 127.31, 127.17, 127.10, 127.07, 127.05, 126.70, 123.07, 123.04, 121.96, 121.94, 121.91, 121.63, 121.59, 111.90, 111.83, 111.44, 111.40, 35.60, 34.32, 34.30, 31.77, 31.23, 31.21, 29.71, 22.70, 19.69, 19.66, 19.48, 19.47, 17.54, 17.48, 17.47, 17.45, 14.20, 14.12. APPI-HRMS (*m/z*): calculated for C₇₆H₄₆D₉N₃O₈Na [M+Na]⁺: 1169.4452, found: 1169.4423.

2-h9. Under a nitrogen atmosphere, **PXX-xy-Bpin** (1.5 eq, 0.222 mmol, 112.6 mg), **Br-NMI-NDI-dtbp** (1 eq, 0.150 mmol, 124.8 mg), and potassium carbonate (2 eq, 0.300 mmol, 41.5 mg) were dissolved in tetrahydrofuran (15 mL) and water (1.5 mL). The mixture was sparged with nitrogen for 15 minutes. The flask was opened briefly to add tetrakis(triphenylphosphine) palladium(0) (0.05 eq, 0.0075 mmol, 8.7 mg), then sparged with nitrogen for another 15 minutes. The mixture was then heated to reflux and stirred 12 h (overnight). After cooling to room temperature, the solvent was removed under reduced pressure. The product was purified with flash chromatography (using 3% ethyl acetate in dichloromethane as the mobile phase), yielding **2-h9** as a yellow-green solid (100 mg, 59%). ¹H NMR (500 MHz, CDCl₃, δ): 8.90-8.82 (m, 4H), 8.76 (dt, J₁ = 7.4 Hz, J₂ = 3.0 Hz, 1H), 8.72 (t, J = 7.7 Hz, 1H), 8.07 (t, J = 7.9 Hz, 1H), 7.82-7.74 (m,

2H), 7.60 (d, $J = 8.7$ Hz, 1H), 7.48 (dd, $J_1 = 8.7$ Hz, $J_2 = 2.3$ Hz, 1H), 7.35 (dd, $J_1 = 9.1$ Hz, $J_2 = 1.9$ Hz, 1H), 7.26-7.19 (m, 3H), 7.14-6.96 (m, 6H), 6.93 (dd, $J_1 = 16.6$ Hz, $J_2 = 9.2$ Hz, 1H), 6.78 (dd, $J_1 = 7.8$ Hz, $J_2 = 2.4$ Hz, 1H), 6.67 (m, 1H), 2.27-2.20 (m, 6H), 2.13 (s, 3H), 2.07 (s, 3H), 1.34-1.32 (m, 9H), 1.28 (s, 9H). ^{13}C NMR (126 MHz, CDCl_3 , δ): 163.93, 163.92, 163.86, 163.74, 163.73, 162.40, 152.65, 152.64, 152.18, 150.40, 147.28, 147.24, 144.54, 144.54, 144.31, 144.29, 143.75, 143.74, 139.55, 139.51, 137.54, 137.49, 135.58, 135.58, 135.26, 135.23, 134.74, 134.69, 134.47, 134.45, 134.41, 134.40, 134.20, 133.64, 133.64, 133.59, 133.58, 133.28, 133.27, 133.19, 133.18, 132.27, 132.25, 132.15, 132.10, 132.06, 131.73, 131.72, 131.61, 131.58, 131.57, 131.51, 131.49, 131.46, 131.38, 131.36, 131.35, 131.33, 130.94, 130.88, 130.82, 129.75, 129.68, 129.04, 129.01, 128.98, 128.12, 128.08, 127.84, 127.72, 127.57, 127.54, 127.50, 127.45, 127.35, 127.31, 127.24, 127.18, 127.10, 127.06, 126.70, 126.61, 126.58, 125.31, 125.21, 123.07, 123.03, 121.96, 121.93, 121.91, 121.63, 121.59, 120.26, 120.24, 117.52, 117.39, 117.38, 111.92, 111.84, 111.45, 111.42, 108.78, 108.64, 108.56, 35.60, 34.32, 34.30, 31.77, 31.23, 31.22, 29.71, 19.70, 19.66, 19.48, 19.47, 17.54, 17.48, 17.47, 17.45. APPI-HRMS (m/z): calculated for $\text{C}_{76}\text{H}_{55}\text{N}_3\text{O}_8$ ESI-HRMS (m/z): calculated for $\text{C}_{76}\text{H}_{55}\text{N}_3\text{O}_8$ $[\text{M}]^+$: 1137.3984, found: 1137.3998.

Optical Spectroscopic Characterization

The two enantiomers of (*R,S*)-**1-h₉** and (*R,S*)-**1-d₉** were separated using a chiral HPLC column (Fig. S3). Their steady-state UV-Vis spectra were obtained with a Shimadzu-1800 spectrophotometer in toluene. The spectrum of racemic (*R,S*)-**1-h₉** along with the spectra of PXX-**h₉**, racemic (*R,S*)-NMI₂, and NDI are shown in Fig. S4a. The spectrum of (*R,S*)-**1-h₉** is approximately an additive combination of those of PXX, (*R,S*)-NMI₂, and NDI, thus indicating that the electronic coupling between these redox components is relatively weak. The corresponding spectra of (*R,S*)-**1-d₉** are nearly identical (Fig. S4c). Circular dichroism (CD) spectra of each enantiomer show the expected mirror image symmetry over the absorption range of the chiral

NMI₂ bridge molecule (Figs. S4b and S4d), which is in full agreement with the CD spectra reported for NMI₂ previously.⁽³²⁾

Details of the transient absorption instrumentation have been described previously.⁽⁵²⁾ Briefly, ~50% of the output of a 1 kHz amplified Ti:sapphire system at 827 nm (1 W, 100 fs, Spitfire, Spectra Physics) is used to pump a non-collinear optical parametric amplifier (TOPAS-Prime, Light-Conversion, LLC.) tuned to generate the ~120 fs, 520 nm pump pulses. The pump is depolarized to minimize polarization-specific dynamics. In the nsTA experiment, the probe is generated in a separately delayed broadband laser system (EOS, Ultrafast Systems, LLC). The transmitted probe is detected on a commercial spectrometer (customized Helios-EOS, Ultrafast Systems, LLC).

Transient absorption (TA) measurements were used to obtain the photoinduced electron transfer dynamics for the racemic mixtures (*R* and *S*)-**1-h₉**, (*R* and *S*)-**1-d₉** as well as the achiral reference molecules **2-h₉** and **2-d₉** in a butyronitrile (PrCN) glass at 105 K using a 120-fs, 450 nm pump pulse and monitoring the transient spectra at 100 fs-250 μs (Fig. S5). These data were globally fit over the entire time range to yield evolution-associated spectra (Fig. S6). Photoexcitation of (*R* and *S*)-**1-h₉** results in the ground state bleach (GSB) of its 450 nm absorption accompanied by the appearance of the excited state absorption (ESA) bands of the lowest excited singlet state of PXX-*h₉* (¹*PXX) at 630, 779, and 1177 nm, as well as stimulated emission features at 483 and 523 nm (Figs. 5a and S6a). These transient features decay in $\tau_{CS1} = 12.4 \pm 0.4$ ps accompanied by the rise of a complex transient signal showing a prominent 979 nm band characteristic of PXX-*h₉*⁺.⁽³¹⁾ The 410 nm absorption characteristic of NMI[•] is largely cancelled out by the PXX-*h₉* GSB.⁽⁵³⁾ A second electron transfer producing NDI[•] occurs in $\tau_{CS2} = 203 \pm 8$ ps as indicated by the formation of the sharp features at 474 and 601 nm.⁽⁵³⁾ Further low amplitude absorption changes of PXX-*h₉*⁺ and NDI[•] occur in $\tau_{rlx} = 32 \pm 5$ ns, which are attributed to a

relaxation process in the low temperature glassy solvent followed by decay of the PXX-*h*₉^{•+}-NDI^{•-} SCRPs to its ground state in $\tau_{\text{CR}} = 65.9 \pm 0.7 \mu\text{s}$. The corresponding TA data for (*R* and *S*)-**1-d**₉ (Figs. S5c and S6c) exhibit spectra and kinetics very similar to those of (*R* and *S*)-**1-h**₉, where the charge recombination time of the PXX-*d*₉^{•+}-NDI^{•-} SCRPs to its ground state $\tau_{\text{CR}} = 51.1 \pm 0.3 \mu\text{s}$.

TA measurements under the same conditions were conducted on the achiral reference molecule **2-h**₉. The transient spectra at selected times are shown in Fig. S5b. The spectral features are very similar to those of (*R* and *S*)-**1-h**₉, and the time constants for charge separation and recombination obtained from the global fits to the data are $\tau_{\text{CS1}} = 4.8 \pm 0.3 \text{ ps}$, $\tau_{\text{CS2}} = 213 \pm 6 \text{ ps}$, $\tau_{\text{rlx}} = 4.8 \pm 0.5 \text{ ns}$, and $\tau_{\text{CR}} = 46.4 \pm 0.6 \mu\text{s}$. The TA data for achiral **2-d**₉ (Figs. S5d and S6d) exhibit spectra and kinetics very similar to those of **1-h**₉, where the charge recombination time of the PXX-*d*₉^{•+}-NDI^{•-} SCRPs to its ground state in $\tau_{\text{CR}} = 57.0 \pm 0.1 \mu\text{s}$. The TA data show that (*R* and *S*)-**1** and **2** have ultrafast charge separation rates, which ensures an initial singlet state precursor, as well as long SCRPs recombination lifetimes, making them excellent candidates for studying the CISS effect on their spin dynamics.

Transient Electron Paramagnetic Resonance (TREPR) Spectroscopy

All EPR measurements were performed at X-band (~9.6 GHz) on a Bruker Elexsys E680 X/W EPR spectrometer equipped with a split ring resonator (ER4118X-MS3). The temperature was maintained at 85 K using an Oxford Instruments CF935 continuous-flow cryostat using liquid nitrogen. The sample was photoexcited at 450 nm with 7 ns, 1 mJ laser pulses generated via an optical parametric oscillator (Spectra-Physics BasiScan) pumped with the 355 nm output of a frequency-tripled Nd:YAG laser (Spectra-Physics Quanta-Ray Lab-170+-10H) operating at a repetition rate of 10 Hz. The laser light was coupled into the resonator via a fiber optic (Thorlabs FT1000UMT) and collimator placed outside the cryostat window.

All EPR measurements were performed in the liquid crystal, 5CB (Sigma-Aldrich). Solutions with an O.D. of 0.5 over a 2 mm pathlength were loaded into quartz tubes (2.40 mm o.d., 2.00 mm i.d.), subjected to three freeze-pump-thaw cycles on a vacuum line (10^{-3} Torr), and sealed with a hydrogen torch. The samples slightly warmed, then aligned in a 1 T magnetic field for 5 minutes and quickly loaded into the already cold resonator at 85 K. Two sample orientations were collected, one, as loaded, with the 5CB director parallel to the magnetic field, and other by rotating the sample 90 degrees to generate a liquid crystal director perpendicular to the magnetic field.

Transient continuous-wave EPR (TREPR) spectra were collected following photoexcitation, the kinetic traces of the transient magnetization at a fixed magnetic field were acquired in quadrature under CW irradiation (0.62 mW). Sweeping the magnetic field gave 2D spectra of magnetic field versus time. For each kinetic trace, the average of the signal acquired prior to the laser pulse was subtracted from the data. The kinetic traces recorded at magnetic field values off-resonance were considered background signals, whose average was also subtracted from all kinetic traces. The spectra were then smoothed in time domain using a Savitzky-Golay filter and appropriately phased into absorption/emission and dispersion. All processing and fitting of the spectra were performed in Matlab using home written scripts and the simulation package EasySpin v6.0-dev.(54, 55)

Out-of-phase electron spin echo envelope modulation (OOP-ESEEM) spectroscopy was collected 50 ns following photoexcitation using a two-pulse, $\pi/2 - \tau - \pi$, pulse sequence. Microwave pulses were generated using a 1 kW TWT amplifier (Applied Systems Engineering 117X) in a partially over-coupled resonator to minimize ringing. Using pulse lengths of $\pi/2 = 16$ ns and $\pi = 32$ ns, the pulse sequence was started at $\tau = 100$ ns and incremented $\Delta\tau = 16$ ns, a standard 4-step phase cycle was utilized and the integrated spin echo intensity was recorded.

The time domain OOP-ESEEM traces were fit with the equation:(38)

$$S(\tau) = e^{-\tau/T_d} \int_0^\pi \sin(J + D(\theta)) \tau W(\theta) \sin \theta d\theta \quad (\text{S1})$$

where T_d is a relaxation time, J is the exchange coupling and $D(\theta)$ is the dipolar coupling and $W(\theta)$ is the weighting function ordering imposed by the liquid crystal. The dipolar coupling takes the form:

$$D(\theta) = \frac{\mu_0}{4\pi h} \frac{g_D g_A \beta_e^2}{r_{DA}^3} (1 - 3\cos^2\theta) \quad (\text{S2})$$

When calculating the distance, g_D and g_A were both taken as the free electron g -value, $g_e = 2.0023$. In the main text we have also introduced the constant $d \equiv \frac{\mu_0}{4\pi h} \frac{g_D g_A \beta_e^2}{r_{DA}^3} = 52.04 \text{ MHz nm}^3 / r_{DA}^3$. The parallel and perpendicular spectra were fit simultaneously with weighting function $W(\theta) = e^{\lambda(3\cos^2\theta - 1)/2}$, where $\lambda = 5$ for the parallel spectra and $\lambda = -5$ for the perpendicular spectra, resulting in an orientation distribution with a FWHM of $\sim 20^\circ$. We have checked that this orientation distribution does not produce a visible effect on the resulting TREPR spectra.

The OOP-ESEEM data and fits are shown in Figs. S7 and S8 and the fitting parameters are summarized in Table S1.

Density Functional Theory Calculations

Geometry optimizations of (*R*)-**1-h₉**, (*S*)-**1-h₉**, and **2-h₉** were performed using density functional theory (DFT) at B3LYP/6-31G* level of theory in QChem (version 5.1).⁽⁵⁶⁾ The optimized structures are shown in Fig. S9 and the optimized cartesian coordinates are given in Tables S2-S4.

Supplementary Text

Spin-Correlated Radical Pair (SCRIP) Theory

SCRIP with no CISS Effect

The radical pair spin Hamiltonian is:

$$\hat{\mathcal{H}} = \beta_e \mathbf{B}_0 g_D \hat{\mathbf{S}}_D + \beta_e \mathbf{B}_0 g_A \hat{\mathbf{S}}_A + J \hat{\mathbf{S}}_D \hat{\mathbf{S}}_A + \hat{\mathbf{S}}_D \mathbf{D}_{DA} \hat{\mathbf{S}}_A + \hat{\mathcal{H}}_{HF} \quad (\text{S3})$$

The first two terms are the electron Zeeman interaction with the static magnetic field, \mathbf{B}_0 ; J is the exchange coupling; \mathbf{D}_{DA} is the electron-electron dipole interaction matrix with principal elements of $[D \ D \ -2D]$ and D follows the definition given in eqn S2; and within the final term, $\hat{\mathcal{H}}_{HF}$, are the electron-nuclear hyperfine interactions.

In the coupled spin basis, $|T_+\rangle, |T_0\rangle, |T_-\rangle, |S\rangle$, this leads to the Hamiltonian matrix:(39, 40, 57)

$$\hat{\mathcal{H}} = \begin{bmatrix} v_+ + \frac{J}{4} + \frac{D}{4} & 0 & 0 & 0 \\ 0 & \frac{J}{4} - \frac{D}{2} & 0 & v_- \\ 0 & 0 & -v_+ + \frac{J}{4} + \frac{D}{4} & 0 \\ 0 & v_- & 0 & -\frac{3J}{4} \end{bmatrix} \quad (\text{S4})$$

where:

$$v_+ = \frac{1}{2}\beta_e(g_D + g_A)B_0 + \sum_j(a_{Dj} + a_{Aj})m_j \quad (\text{S5a})$$

$$v_- = \frac{1}{2}\beta_e(g_D - g_A)B_0 + \sum_j(a_{Dj} - a_{Aj})m_j \quad (\text{S5b})$$

The angle θ follows the standard definition, the angle between the vector connecting the two spins and the laboratory magnetic field. More generally, the Hamiltonian matrix, eq. S4, is written in the laboratory frame as defined by the high-field approximation. It is readily apparent that the off-diagonal term, v_- , (i.e. the difference between the effective Zeeman energies of the two ions, also including the contribution from hyperfine couplings) will mix the $|T_0\rangle$ and $|S\rangle$ states and upon diagonalization yields the eigenstates:

$$\begin{aligned} |1\rangle &= |T_{+1}\rangle \\ |2\rangle &\equiv |\Phi_A\rangle = \cos \phi |S\rangle + \sin \phi |T_0\rangle \\ |3\rangle &\equiv |\Phi_B\rangle = -\sin \phi |S\rangle + \cos \phi |T_0\rangle \\ |4\rangle &= |T_{-1}\rangle \end{aligned} \quad (\text{S6})$$

when

$$\phi = \frac{1}{2} \tan^{-1} \frac{2v_-}{D/2 - J} \quad (\text{S7})$$

And the eigenvalues:

$$\begin{aligned}
 E_1 &= \nu_+ + \frac{(J+D)}{4} \\
 E_2 &= -\frac{(J+D)}{4} + \sqrt{\left(\frac{J}{2} - \frac{D}{4}\right)^2 + \nu_-^2} \\
 E_3 &= -\frac{(J+D)}{4} - \sqrt{\left(\frac{J}{2} - \frac{D}{4}\right)^2 + \nu_-^2} \\
 E_4 &= -\nu_+ + \frac{(J+D)}{4}
 \end{aligned} \tag{S8}$$

The spin Hamiltonian and its resulting eigenvalues and eigenvectors are independent of any molecular chirality and only depend on the magnetic properties of the involved spins.

The steady-state EPR spectrum (after coherences are lost) in field or frequency space is composed of peaks at positions determined by differences in the eigenvalues of the spin Hamiltonian, eqns. S8, with intensities determined by the transition rate between the eigenstates $|i\rangle$ and $|j\rangle$ and their population differences:

$$I_{ij} \propto |\langle i|\hat{S}_y|j\rangle|^2 (p_i - p_j) \tag{S9}$$

where p_i and p_j are the populations of the two eigenstates which correspond to the diagonal elements of the density matrix in the eigenbasis and depend upon on the initial state, i.e. $p_i = |\langle i|\psi_0\rangle|^2$. $\langle i|\hat{S}_y|j\rangle$ is the magnetic dipole matrix element of the examined transition along the direction of the microwave field, which is orthogonal to the static field.

Conversely, transition frequencies (and hence peak positions) only depend on the Hamiltonian eigenvalues and not on the specific initial state.

The four transitions of the SCRP (starting from a singlet precursor) appear at their usual positions.

All four transitions are of the same intensity (see definition in Eq. S9) such that:

$$I_{12} = -I_{24} = I_{13} = -I_{34} = \frac{\cos^2 \phi \sin^2 \phi}{2} = \frac{\nu_-^2}{2(D/2-J)^2 + 8\nu_-^2} \tag{S10}$$

SCRP with the CISS Effect

The state for a radical pair following electron transfer through a chiral bridge can be written as

$$|\psi_0\rangle = \cos \chi |S\rangle + \sin \chi |T_0(\mathbf{n})\rangle \tag{S11}$$

This state was first proposed by Luo and Hore,⁽⁴⁶⁾ where the angle χ is related to the chirality and quantifies the effect of CISS in the reaction. The states $|S\rangle$ and $|T_0(\mathbf{n})\rangle$ are the radical pair singlet and the radical pair triplet states, respectively; in particular, the triplet state is defined with respect to the axis \mathbf{n} of charge separation, which is also the axis of chirality, the CISS quantization axis, and the long molecular axis. In the limiting cases: $\chi = 0$ (no CISS), $|\psi_0\rangle$ is a pure singlet state; at the other extreme $\chi = \pm\frac{\pi}{4}$, so that $|\psi_0\rangle = |\uparrow\downarrow(\mathbf{n})\rangle$ or $|\downarrow\uparrow(\mathbf{n})\rangle$, i.e. it shows maximum local spin polarization (100% CISS); and when $\chi = \pm\frac{\pi}{2}$, $|\psi_0\rangle = |T_0(\mathbf{n})\rangle$ a pure triplet state. The \pm refers to the two different enantiomers.

In the basis of the spin Hamiltonian, eqn. S4, the triplet state is defined in the high-field limit and polarized along the laboratory magnetic field. When working in orientations or distributions of orientations where the CISS axis is not aligned with the laboratory magnetic field, it becomes necessary to rotate the state as defined in the molecular frame to the laboratory frame:

$$e^{-i\hat{S}_y\theta}|\psi_0\rangle = |\psi_0(\theta)\rangle = \cos\chi|S\rangle + \sin\chi\left[\cos\theta|T_0\rangle + \frac{\sin\theta}{\sqrt{2}}(|T_{-1}\rangle - |T_{+1}\rangle)\right] \quad (\text{S12})$$

where the singlet component is rotationally invariant, while $|T_0(\mathbf{n})\rangle \equiv |T_0(\theta)\rangle = \cos\theta|T_0\rangle + \frac{\sin\theta}{\sqrt{2}}(|T_{-1}\rangle - |T_{+1}\rangle)$. Similar to eqn. S2, θ is defined as the angle between the CISS axis and the magnetic field. In the $D^+-B\chi-A^-$ molecules studied here, the CISS axis and the dipolar axis are nearly collinear so θ in eqns. S2 and S12 refers to the same measure. When $\theta \neq 0$, sizable components on $|T_{-1}\rangle$ and $|T_{+1}\rangle$ are introduced (see Fig. 3 of the main text).

Let us now focus on the two limiting cases examined in this work, i.e. $\theta = 0^\circ$ and $\theta = 90^\circ$.

The resulting intensity for I_{13} and I_{34} at $\theta = 90^\circ$ is given by:

$$I_{13} = -I_{34} = \frac{1}{4}\cos^2\phi(\cos 2\chi - \cos^2\chi \cos 2\phi) \quad (\text{S13})$$

Showing a dependence on the composition of the eigenstates (ϕ) and on the amount of CISS (χ).

This can be separated into a singlet (I_S) and a 100% CISS (I_{CISS}) contributions, i.e.

$$\begin{aligned} I_{13} = -I_{34} &= \frac{1}{2}(1 - 2 \sin^2 \chi) \cos^2 \phi \sin^2 \phi - \frac{1}{4} \sin^2 \chi \cos^2 \phi \cos 2\phi \\ &= (1 - p) I_S + p I_{CISS} \end{aligned} \quad (\text{S14})$$

where $p = 2 \sin^2 \chi$ represents the CISS efficiency and

$$I_S = \frac{1}{2} \cos^2 \phi \sin^2 \phi \quad (\text{S15})$$

$$I_{CISS} = -\frac{1}{8} \cos 2\phi \cos^2 \phi \quad (\text{S16})$$

Note that for this orientation I_S and I_{CISS} have opposite signs and that I_{CISS} is the same that would be obtained starting from a fully polarized initial state ($\chi = \pm\pi/4$).

The calculation is perfectly analogous for $I_{12} = -I_{24}$, so that

$$I_{12} = -I_{24} = \frac{1}{4} \sin^2 \phi (2 \cos^2 \phi \cos^2 \chi - \sin^2 \chi) \quad (\text{S17})$$

This can also be decomposed into singlet and 100% CISS contributions, with the same sign. Remarkably, in the present case I_{12} and I_{24} are much weaker and occur in the central part of the spectrum. Hence, we focus on the main peaks I_{34} and I_{13} in the following. Similar expressions can also be derived for $\theta = 0$. A summary of the different singlet and CISS contributions for each orientation is reported in Table S5.

In Table S5, blue (orange) indicate emissive (absorptive) signals, fixed by the sign of D . Note that opposite enantiomers are indistinguishable when $\theta = 90^\circ$, while they give different intensities when $\theta = 0^\circ$, which are therefore averaged in the Table S5.

For these specific directions the same results could be obtained using the initial mixed state for electron transfer through a chiral bridge proposed by Chiesa et al.(47) or the coherent superposition

$$|\psi'_0\rangle = \cos \chi |S\rangle + i \sin \chi |T_0(\mathbf{n})\rangle \quad (\text{S18})$$

derived by Fay.(45) Eq. S18 does not yield any single-spin polarization, but was expanded later by Fay(44) to account for spin-spin exchange interactions during multi-step electron transfer processes, leading to polarization effects similar to those postulated by Luo and Hore(46) (a mixture of states S18 and S11 with the same angle χ). Since the three models are equivalent for describing the TREPR spectra, we mainly focus on Eq. S11.(46)

TREPR Spectral Linewidths

To understand how the entanglement of the eigenstates affects the linewidths for different initial states, let us focus again on $\theta = 90^\circ$ and transition I_{13} between $|\Phi_B\rangle$ and $|T_{+1}\rangle$, which occurs on the low field side of the spectrum. Analogous reasoning holds for transition I_{34} on the high field side of the spectrum. The intensities of the transitions for singlet and 100% CISS initial states are given by Eqs. S15 and S16 above. Their dependence on the mixing angle ϕ is very different, as shown in Fig. S10. In order to better compare the linewidths of the two curves, here we report the absolute value of I_S and I_{CISS} (Fig. S10A), along with its derivative (Fig. S10B).

As discussed in the main text, ϕ can be varied by considering different configurations of the nuclear spins coupled to the SCRPs or by distributions of the Hamiltonian parameters. In the present calculations, we included a 14% strain in the donor-acceptor distance, leading to a distribution of dipole-dipole interactions. This, in turn, corresponds to resonances occurring at different values of B_0 . As a result, we can have regions in the tails of a specific peak, which correspond to more entangled states, i.e. such that ϕ is closer to 0 compared to the center of the peak. In this case, moving from the center of the peak to the tail corresponds to moving toward $\phi = 0$ in Fig. S10B, where $d|I_{\text{CISS}}|/d\phi$ is positive and $d|I_S|/d\phi$ is negative. Such a situation, in which I_{CISS} increases while I_S decreases from the center to the tail of the peak leads to a larger broadening of I_{CISS} compared to I_S , thus exactly producing CISS features in the tail when I_{CISS} and I_S are combined.

TREPR Spectral Simulations

The time dependence of the TREPR spectra is simulated by numerically integrating the stochastic Liouville equation for the system density matrix

$$\frac{d\rho_r(\Omega, t)}{dt} = -i \left[\frac{1}{\hbar} \tilde{H}(\Omega) + i\tilde{R} + i\tilde{K} \right] \rho_r(\Omega, t) \quad (\text{S19})$$

where $\rho_r(\Omega, t)$ is the density matrix of the system in the rotating frame, $\tilde{H}(\Omega)$, \tilde{R} and \tilde{K} are super-operators associated to the coherent Hamiltonian evolution, to dephasing/relaxation and recombination effects, respectively. Both relaxation and recombination are negligible in the time range of interest and we therefore omit them in the following. Conversely, off-diagonal elements of ρ_r are affected by pure dephasing, parametrized by transition-dependent T_2 .

Note that in the high-field limit, the non-secular terms in the Hamiltonian are also negligible and the rotating-frame Hamiltonian (including the microwave field) becomes time independent. Hence, Eq. S19 can be directly integrated, leading to

$$\rho_r(\Omega, t) = \exp \left[-\frac{i}{\hbar} \tilde{H}(\Omega) + \tilde{R} + \tilde{K} \right] t \rho_r(\Omega, 0) \quad (\text{S20})$$

from which the spectrum $\langle S_y(B_0, t) \rangle = \text{Tr}[\rho_r(\Omega, t) S_y]$ is calculated.(47)

Apart from the rise of the signal at short times, the resulting spectra are equivalent to those obtained from linear-response theory in the stationary limit, Eq. S9, using, for instance, the Easyspin package for spin-polarized initial states.(54, 55)

The time and field dependencies of the TREPR spectra simulated for the protonated compound using the minimal model described in the main text and simulated for the deuterated case including a distribution of hyperfine fields generated by the four ^1H and two ^{14}N nuclear spins of NDI $^{\cdot-}$ are reported in Figs. S11 and S12. The experimental spectra are very well reproduced, both for the main peaks and for the characteristic CISS features at the two wings. The latter show practically the same time dependence as the main peaks, indicating that they are not transient but resonant

peaks (also present in the steady-state spectra). The full distributions of hyperfine fields, g-tensors and dipolar strain included in this model are slightly different from those reported in the main text, but these small differences do not affect the origin of CISS features.

Electron Transfer Rates and Energetics

The free energies of reaction for (*R* or *S*) **1-h₉** (**-d₉**) and **2-h₉** (**-d₉**) were determined from the modified Weller equation(58) (Eq. S21) using the one-electron oxidation potential $E_{1/2}^+$ of PXX (0.81 V vs. SCE(31), and the one-electron reduction potentials $E_{1/2}^-$ of NMI, NMI₂, and NDI (-1.4 V, (53) -1.5 V(59) and -0.48 V (53) vs SCE, respectively), the estimated dielectric constant of PrCN at 105 K ($\epsilon = 2.3$),(60) and the center-to-center radical ion pair distances given in Table S1 determined as noted. The ionic radii are estimated as half of the donor-acceptor distance and e_0 is the charge of the electron.

$$\Delta G_{DA} = E_{1/2}^+ - E_{1/2}^- + \frac{e_0^2}{\epsilon} \left(\frac{1}{2r_D} + \frac{1}{2r_A} - \frac{1}{r_{DA}} \right) \quad (\text{S21})$$

The values of the electronic coupling matrix elements for the electron transfer reaction were determined using the semi-classical expression for the electron transfer rate k_{ET} given in Eq. S22, (60) where ΔG_{DA} and k_{ET} are the free energies of reaction and measured rate constants given in Table S1. The values of k_{ET} are obtained from the data presented in Figs. S5 and S6. In addition, the total internal reorganization for the one-electron oxidation of PXX and reduction of NMI, NMI₂ or NDI (λ_i) is estimated as 0.5 eV, while the solvent reorganization energy of PrCN at 105 K (λ_s) is estimated from Eq. S23(60) and we make the usual assumption of one dominant vibration ($\omega = 1500 \text{ cm}^{-1}$) coupled to the reaction coordinate of the electron transfer reaction.

$$k_{ET} = \frac{2\pi}{\hbar} V_{DA}^2 \frac{1}{(4\pi\lambda_s k_B T)^{1/2}} \sum_{m=1}^{\infty} \frac{s^m e^{-s}}{m!} \cdot \exp \left[-\frac{(\lambda_s + \Delta G_{DA} + m\omega)^2}{4\lambda_s k_B T} \right] \quad (\text{S22})$$

where $s = \lambda_i/\omega$

$$\lambda_s = e_0^2 \left(\frac{1}{2r_D} + \frac{1}{2r_A} - \frac{1}{r_{DA}} \right) \left(\frac{1}{n^2} - \frac{1}{\epsilon} \right) \quad (\text{S23})$$

where n is the refractive index of the solvent and the remaining values are defined above.

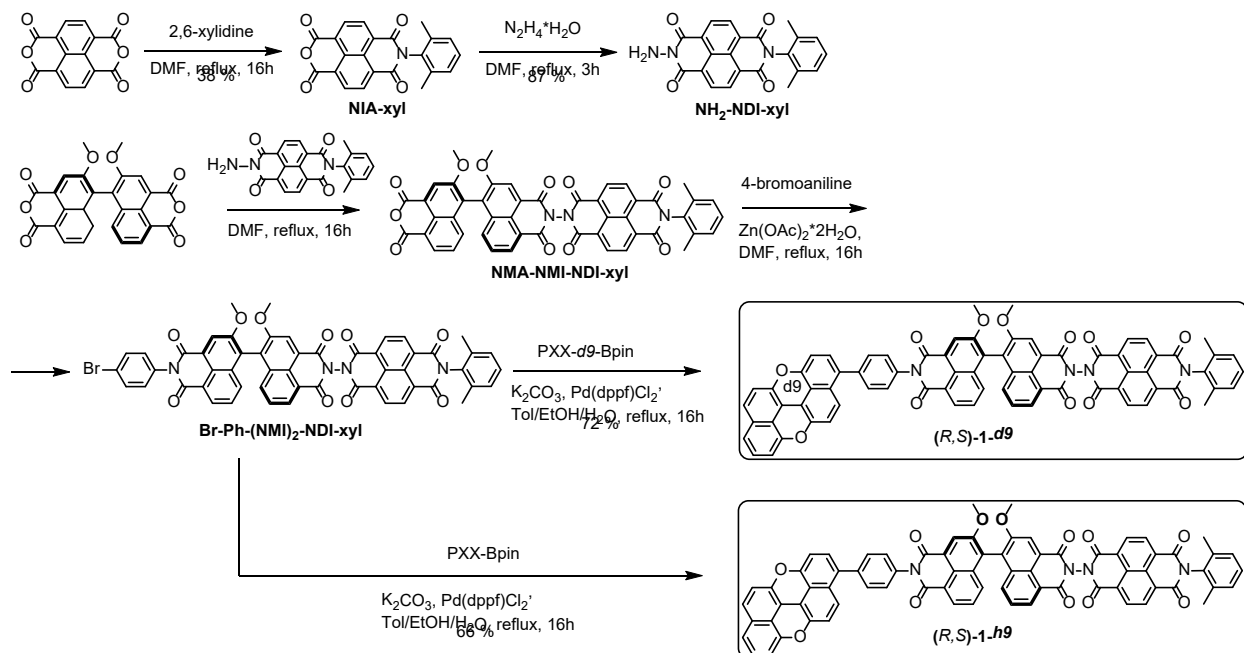


Fig. S1. Synthetic scheme for (R and S)-1-h₉ and (R and S)-1-d₉

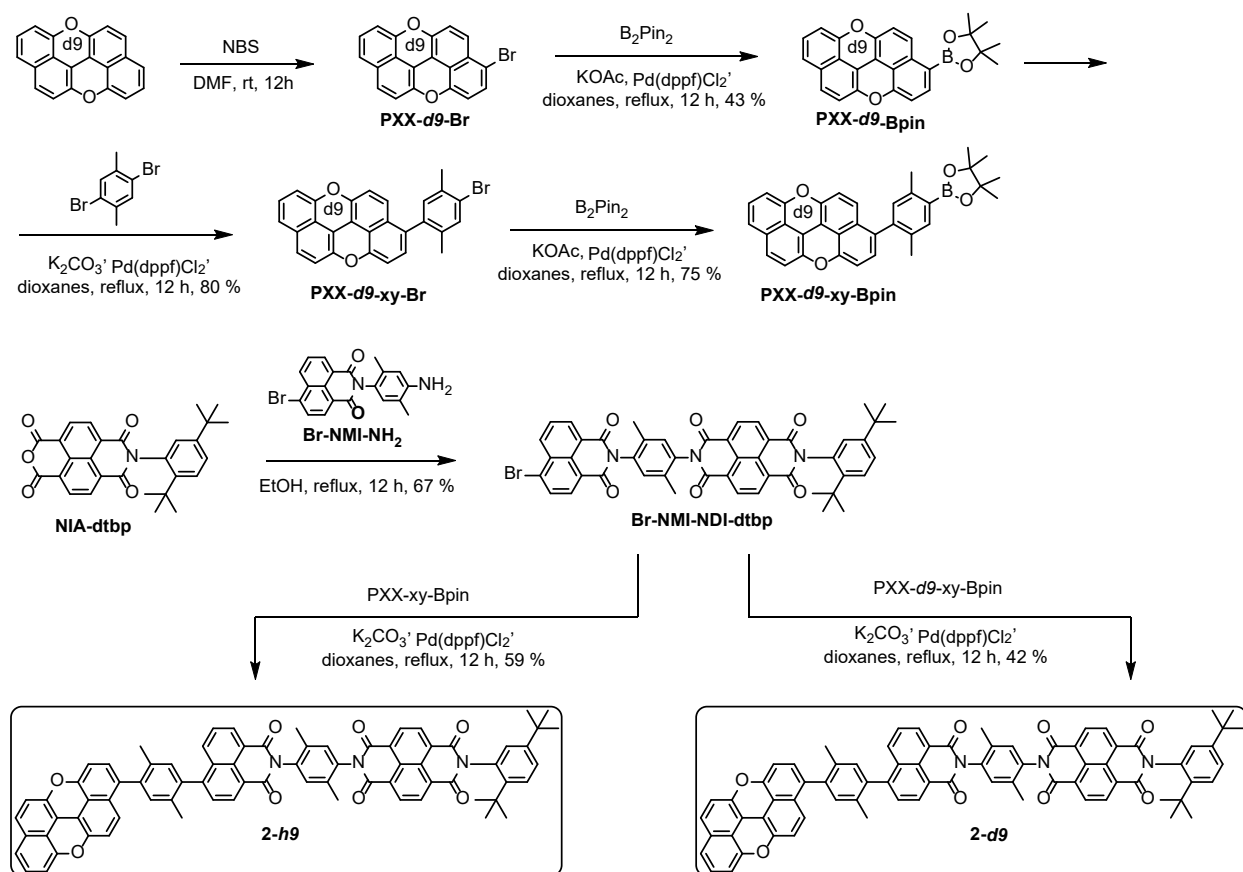


Fig. S2. Synthetic scheme for **2-h₉** and **2-d₉**

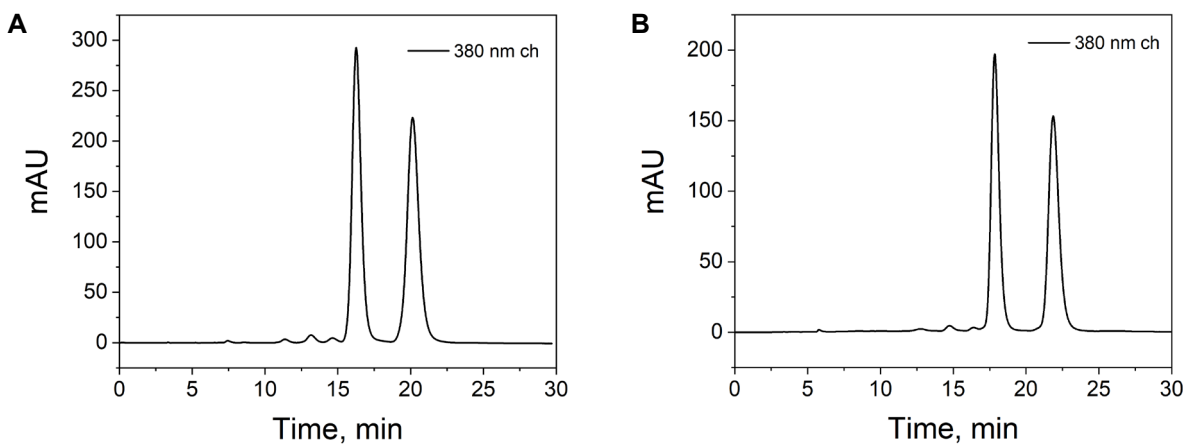


Fig. S3. HPLC chromatogram showing the chiral resolution of (A) (*R* and *S*)-**1-h₉** and (B) (*R* and *S*)-**1-d₉** enantiomers on a ChiralPak IA-3 column (250 x 4.6 mm, 3 μ m) monitored at 380 nm using a dichloromethane/hexanes/isopropanol mixture as an eluent (50/45/5 volume %) at 1 mL/min flow rate. Peaks with the shorter retention times are the (*S*) enantiomers.

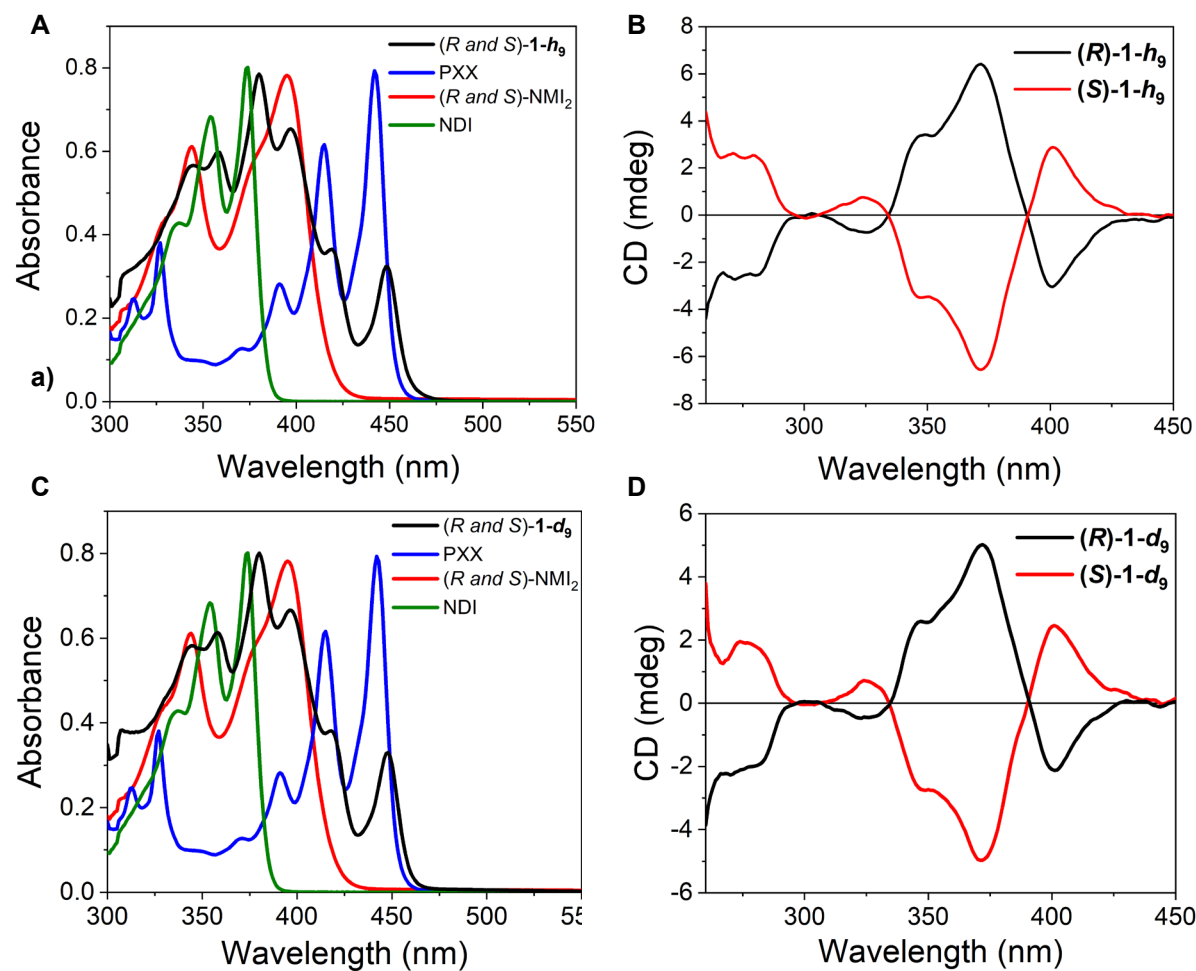


Fig. S4. Optical spectra. (A) UV-vis absorption of the racemic mixture of $(R$ and S)- $1-h_9$, PXX, $(R$ and S)- NMI_2 and NDI in toluene at 295 K. (B) CD spectra of (R) - $1-h_9$ and (S) - $1-h_9$. (C) UV-vis absorption of the racemic mixture of $(R$ and S)- $1-d_9$, PXX, $(R$ and S)- NMI_2 and NDI in toluene at 295 K. (D) CD spectra of (R) - $1-d_9$ and (S) - $1-d_9$.

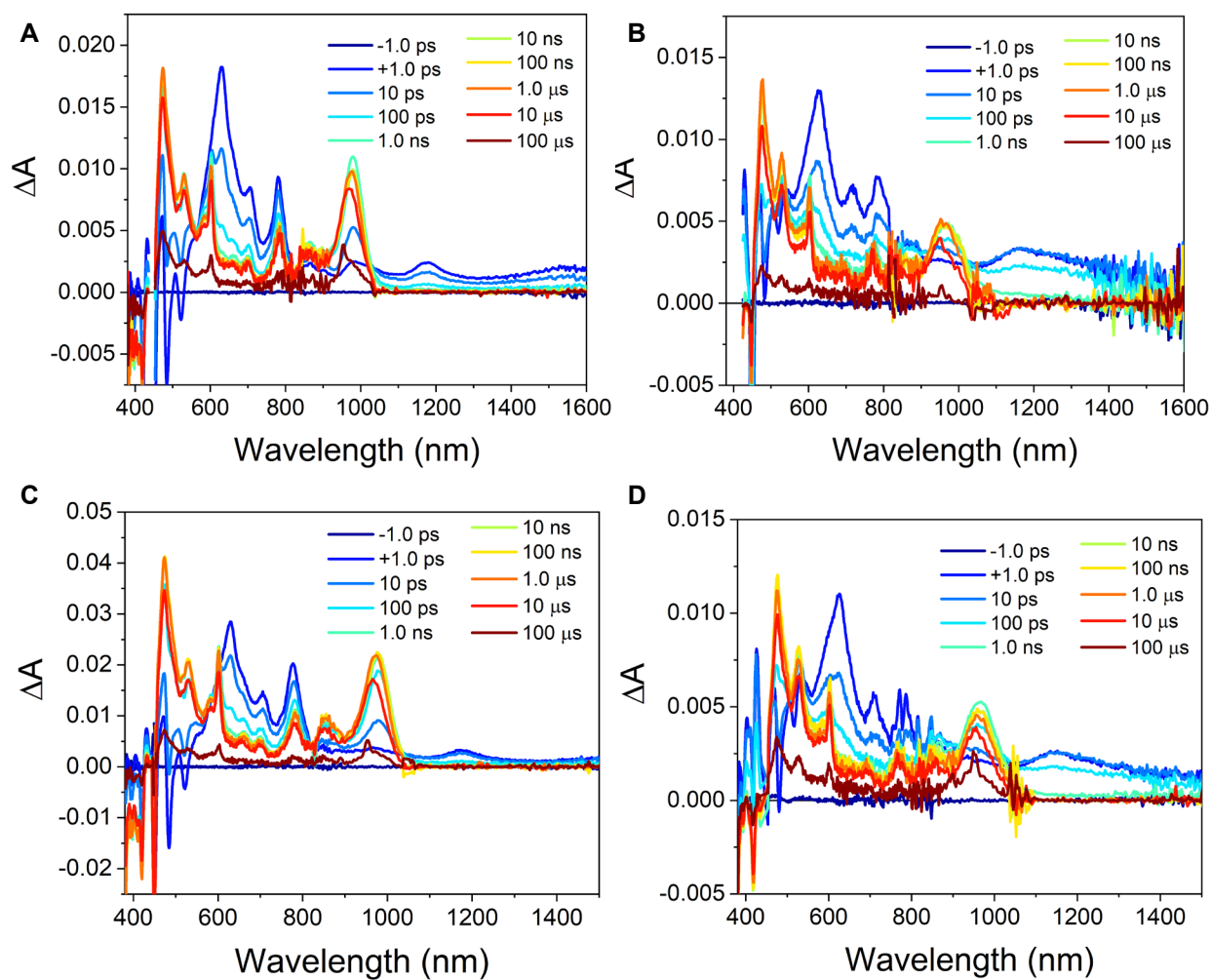


Fig. S5. Transient absorption data following 450 nm excitation of compounds in PrCN at 105 K at the indicated pump-probe delay times. (A) (*R* and *S*)-**1-h**, (B) **2-h**, (C) (*R* and *S*)-**1-d**, (D) **2-d**.

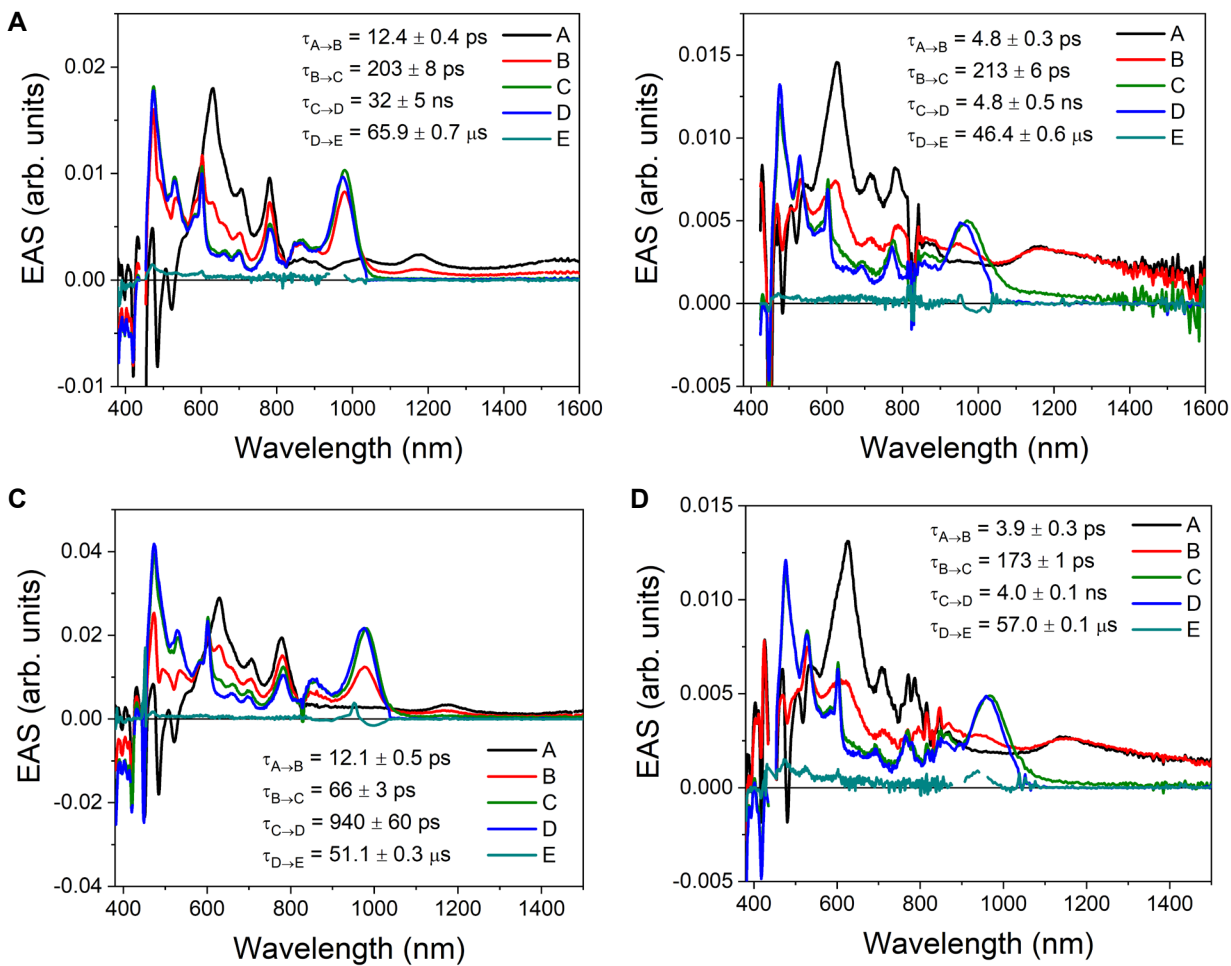


Fig. S6. Evolution-associated spectra obtained by globally fitting the femto- and nanosecond transient absorption data for (A) (*R* and *S*)-1-*h*₉, (B) 2-*h*₉, (C) (*R* and *S*)-1-*d*₉, and (D) 2-*d*₉, following 450 nm excitation in PrCN at 105 K.

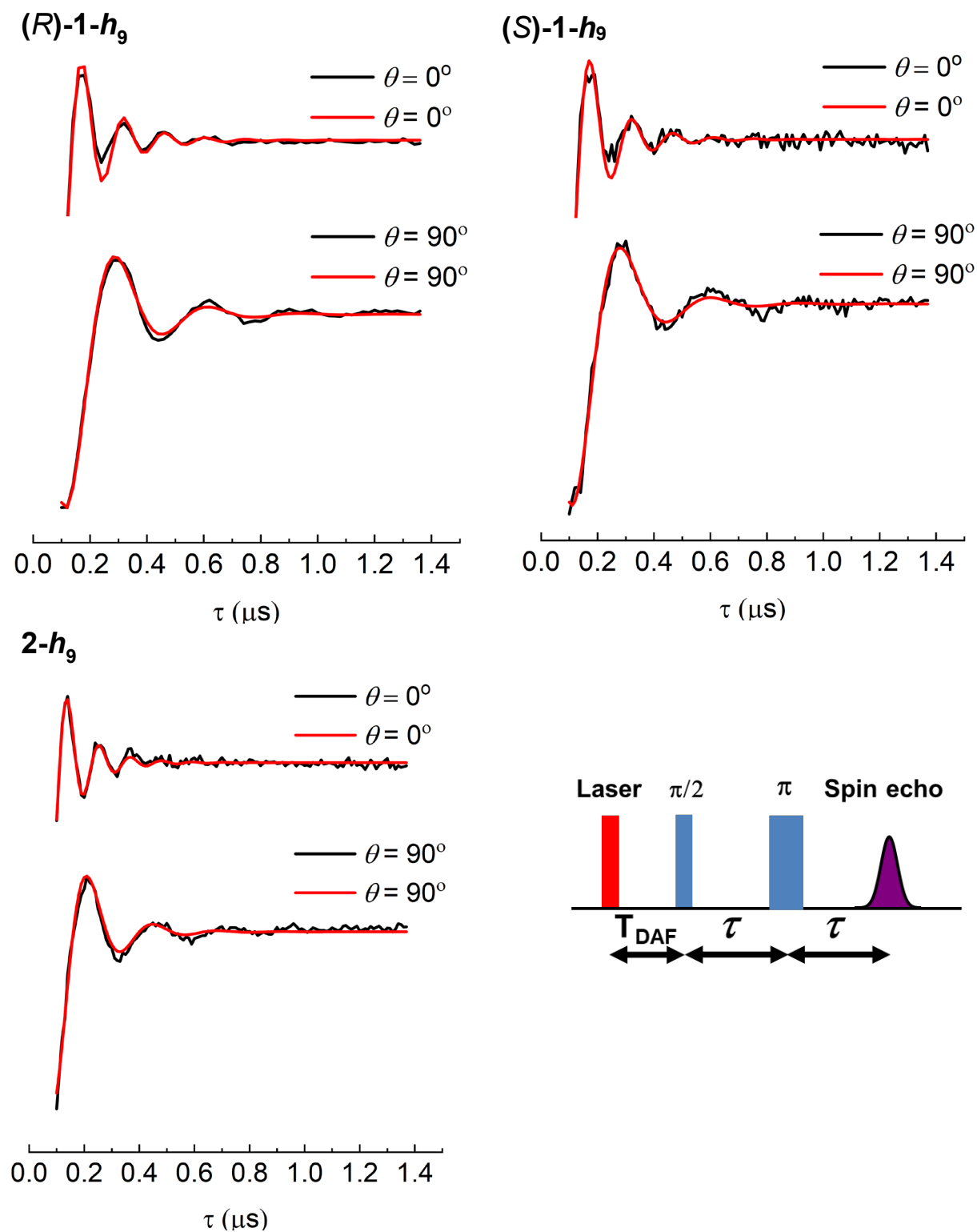


Fig. S7. OOP-ESEEM data and fits at $\theta = 0^\circ$ and $\theta = 90^\circ$ for the indicated molecules oriented in 5CB. Lower right: Hahn echo pulse sequence for OOP-ESEEM experiments, where T_{DAF} is the delay after the laser flash.

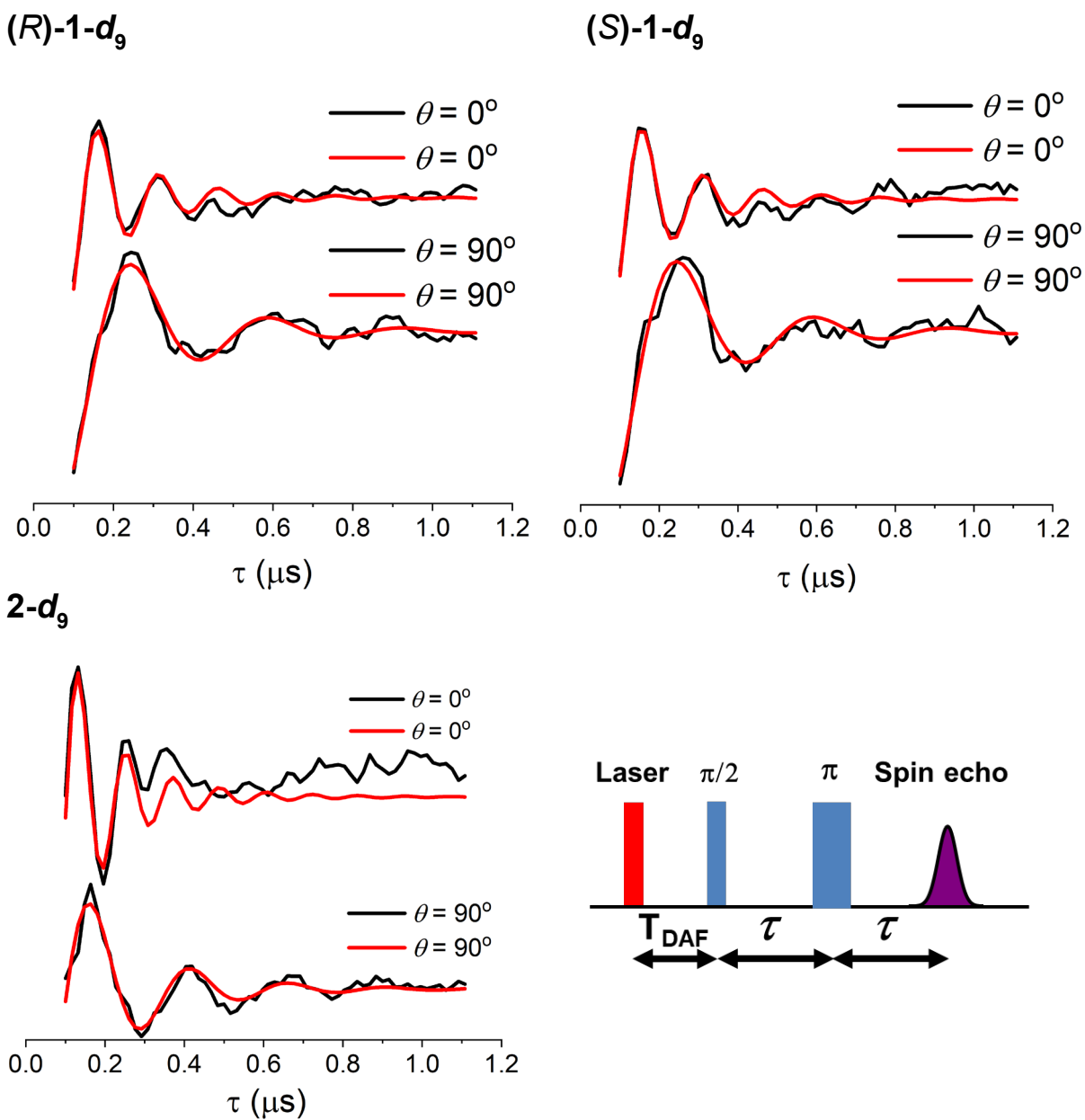
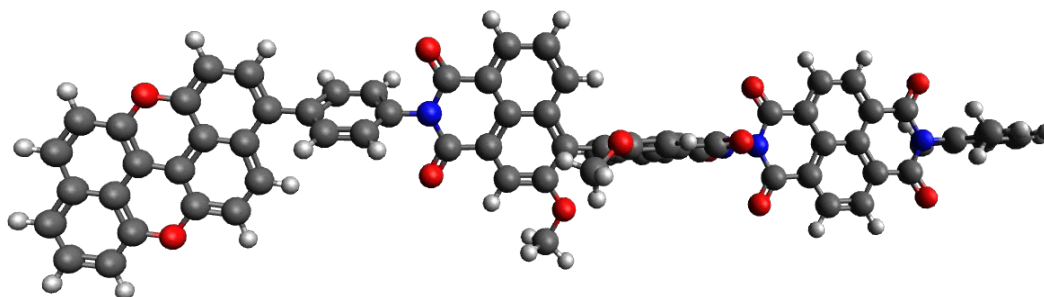
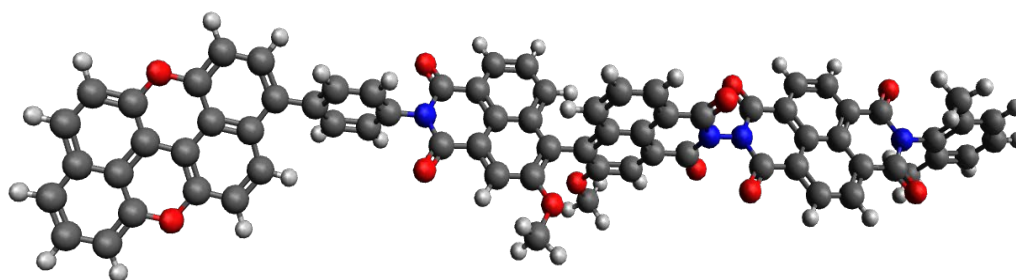


Fig. S8. OOP-ESEEM data and fits at $\theta = 0^\circ$ and $\theta = 90^\circ$ for the indicated molecules oriented in 5CB. Lower right: Hahn echo pulse sequence for OOP-ESEEM experiments, where T_{DAF} is the delay after the laser flash.

A



B



C

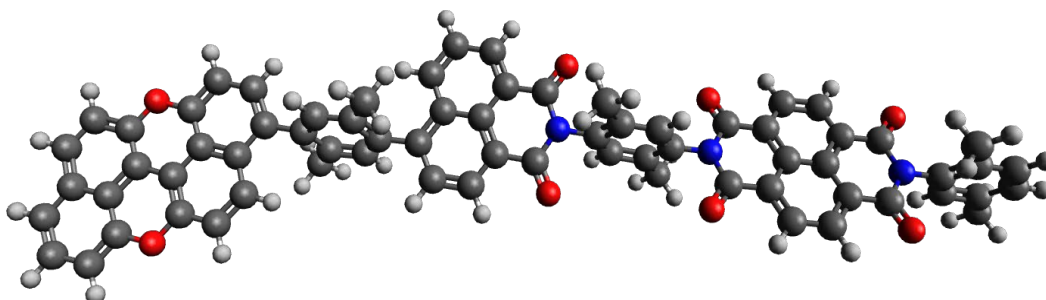


Fig. S9. Geometry optimized structures. (A) (*R*)-1-*h*₉, (B) (*S*)-1-*h*₉, and (C) 2-*h*₉ obtained using density functional theory (DFT) at the B3LYP/6-31G* level of theory in QChem (version 5.1).

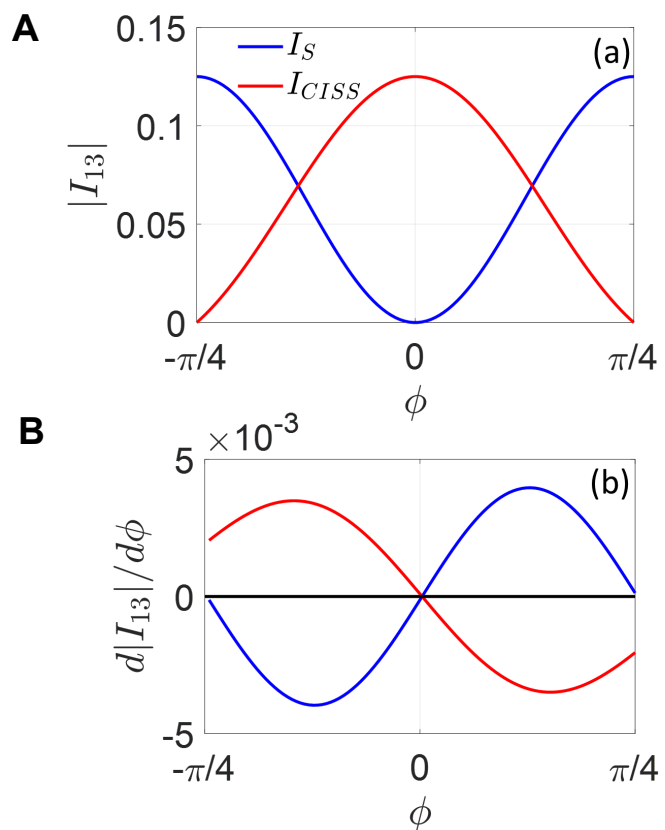


Fig. S10. Transition intensity as a function of the CISS contribution. (A) Dependence of the absolute value of the intensity of the $|\Phi_B\rangle \leftrightarrow |T_{+1}\rangle$ (1-3) transition on the composition of the eigenstates, expressed by the angle ϕ , for an initial singlet (blue line) or fully polarized (100% CISS, red curve) state. (B) Same for its derivative.

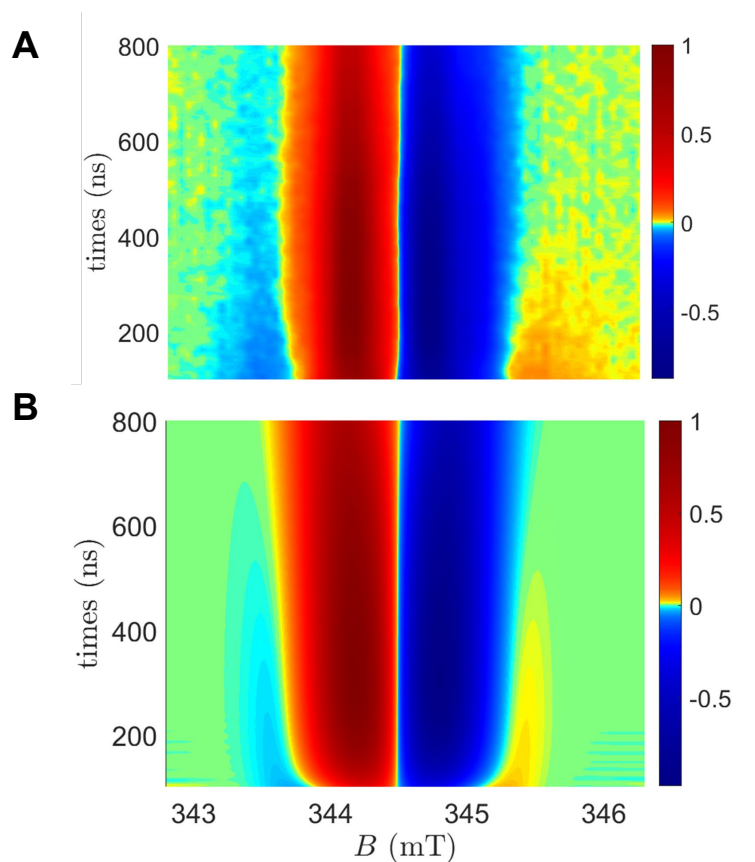


Fig. S11. Time and field dependence of TREPR spectra. Experimental (**A**) and simulated (**B**) time and field dependence of TREPR spectra of (*R* and *S*)-**1-h**₉ with the long axis of each molecule perpendicular to the applied magnetic field direction. The time dependence of the lateral CISS features is enhanced using a non-linear color-scale.

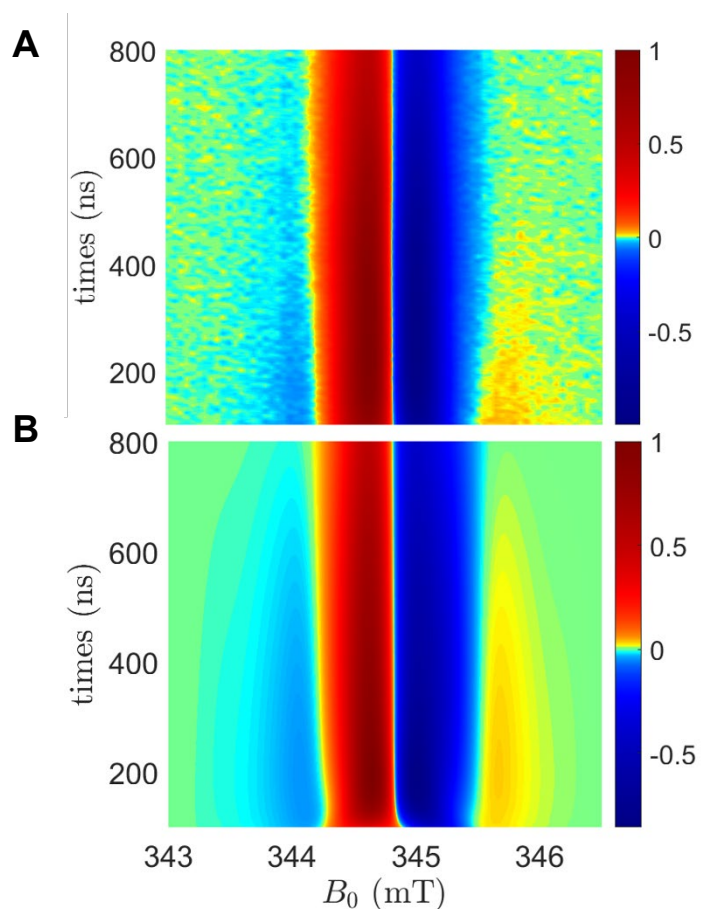


Figure S12. Time and field dependence of TREPR spectra. Experimental (A) and simulated (B) time and field dependence of TREPR spectra of (*R* and *S*)-1-*d*₉ with the long axis of each molecule perpendicular to the applied magnetic field direction. The time dependence of the lateral CISS features is enhanced using a non-linear color-scale. The effect of hyperfine interactions is included as a secular term in the Hamiltonian, with four ¹H (*I* = 1/2) and two ¹⁴N (*I* = 1) nuclear spins coupled to NDI^{•-} with isotropic $a_H = 4$ MHz and $a_N = 2$ MHz. For each configuration of the nuclear spins, we consider a distribution of hyperfine fields with a gaussian broadening of 1 MHz to account for possible strain and anisotropy of the hyperfine couplings. A distribution of donor-acceptor distances with standard deviation 0.5 nm was also included. Slightly different values of the *g*-tensors compared to the minimal model were used $g_{NDI} = (2.0034, 2.0041, 2.0043)$, $g_{PXX} = (2.0032, 2.0046, 2.0046)$ and a CISS contribution of 47 %.

Compound	Electron Transfer Reaction	r_{DA} (nm)	ΔG_{DA} (eV)	k_{ET} (s ⁻¹)	V_{DA} (cm ⁻¹)
(<i>R</i> or <i>S</i>) 1-<i>h</i> (<i>R</i> or <i>S</i>) 1-<i>d</i>	¹ *PXX-NMI ₂ -NDI→ PXX ^{•+} -NMI ₂ ^{•-} -NDI	1.46 ^a	-0.26	8.1 x 10 ¹⁰ 8.3 x 10 ¹⁰	18 18
(<i>R</i> or <i>S</i>) 1-<i>h</i> (<i>R</i> or <i>S</i>) 1-<i>d</i>	PXX ^{•+} -NMI ₂ ^{•-} -NDI→ PXX ^{•+} -NMI ₂ -NDI ^{•-}	2.48 ± 0.01 ^b	-1.09	4.9 x 10 ⁹ 1.5 x 10 ¹⁰	40 70
2-<i>h</i> 2-<i>d</i>	¹ *PXX-NMI-NDI→ PXX ^{•+} -NMI ^{•-} -NDI	1.21 ^a	-0.21	2.1 x 10 ¹¹ 2.6 x 10 ¹¹	74 83
2-<i>h</i> 2-<i>d</i>	PXX ^{•+} -NMI ^{•-} -NDI→ PXX ^{•+} -NMI-NDI ^{•-}	2.28 ± 0.01 ^b	-1.12	4.7 x 10 ⁹ 5.8 x 10 ⁹	18 20

Table S1. Electron Transfer Data. ^aDistances obtained from the DFT calculations given in Tables S3-S5. ^bDistances obtained from the OOP-ESEEM data given in the main text.

Compound	J (MHz)	r_{DA} (nm)
<i>(S)</i> - 1-h₉	-0.21 ± 0.09	2.48 ± 0.01
<i>(R)</i> - 1-h₉	-0.28 ± 0.11	2.48 ± 0.01
2-h₉	-0.14 ± 0.10	2.28 ± 0.01
<i>(S)</i> - 1-d₉	-0.31 ± 0.10	2.53 ± 0.01
<i>(R)</i> - 1-d₉	-0.18 ± 0.10	2.51 ± 0.01
2-d₉	-0.25 ± 0.10	2.29 ± 0.01

Table S2. OOP-ESEEM fit parameters

(R)-1h₉

Coordinates (Angstroms)

ATOM	X	Y	Z
1 H	16.3358942944	-4.3281626064	-2.2877779347
2 H	18.8019623042	-4.1693433187	-1.9479313717
3 C	16.7611601820	-3.5145988373	-1.7095809383
4 C	18.1587795359	-3.4119561690	-1.5083550495
5 O	14.5660393913	-2.6739519154	-1.3610844712
6 H	11.9554419289	-2.7139744068	-1.5808736086
7 C	15.9315444646	-2.5615966536	-1.1581652039
8 H	6.7328227085	1.1956699080	2.5948679097
9 C	12.3283682942	-1.8685093007	-1.0113134439
10 C	18.7163833194	-2.3845926757	-0.7749051188
11 H	9.1962546309	1.1050068920	2.8402936355
12 C	13.7165528883	-1.7324192465	-0.8150725568
13 H	19.7921984943	-2.3275352957	-0.6334012584
14 C	16.4771104203	-1.4935031639	-0.3987795457
15 C	11.4606382462	-0.9370578779	-0.4711447059
16 H	-16.6065064634	-2.6405937900	2.4174190066
17 C	7.3691531102	1.2034762054	1.7159872678
18 C	-1.8269945346	-0.5152290510	0.2083806265
19 C	17.8825534162	-1.3907657745	-0.1961869238
20 C	-3.2551505378	-0.4921919533	0.1830938352
21 H	10.3942787638	-1.0680207988	-0.6182288983
22 C	8.7541789852	1.1581587223	1.8496320274
23 C	14.1997169495	-0.6752613331	-0.0733415615
24 O	-6.0321160099	1.1785465171	-1.5033436950
25 H	1.6450232955	-3.3923115486	-1.3680027496
26 C	-15.8988961538	-2.0526615079	1.8260684184
27 C	15.6076544587	-0.5298791633	0.1585942148
28 H	-15.2557354228	-1.5043821588	2.5250233216
29 H	-15.2645627919	-2.7546285296	1.2714685306
30 C	11.9189161302	0.1811046448	0.2893023948
31 C	18.3494238737	-0.2892156097	0.5804127404
32 C	13.3273161708	0.2848801528	0.4886757962
33 C	2.5580440635	-0.7477155995	-0.9855300313
34 C	3.2308530614	0.3068324835	-0.3978768148
35 C	4.7117015711	0.2278505312	-0.2925212371
36 C	3.2246847375	2.5106941690	0.6817524741
37 C	2.5239245555	1.4266326195	0.0935108442
38 C	4.7040872449	2.4832567201	0.7968925806
39 C	1.1519314424	-0.7219852159	-1.0951769561
40 C	2.5343610706	3.6077804483	1.1614267250
41 C	1.1250477687	-2.8658485725	-2.1775722624
42 O	5.3427683922	-0.7345995100	-0.7007680978
43 C	1.0964757572	1.4573806069	-0.0020593889
44 C	1.1273931851	3.6459799453	1.0751780471
45 C	0.4241377198	2.6007817471	0.5143995436

46	C	0.4108253560	0.3559605914	-0.5997675805
47	N	5.3586783224	1.3246848202	0.3099582008
48	O	5.3426153314	3.3978093410	1.2893845788
49	O	0.4381285903	-1.7149465830	-1.6950858853
50	C	6.7970869904	1.2652523619	0.4464860312
51	C	-1.0813041063	0.3342850776	-0.6792930564
52	H	3.1449148758	-1.5798425606	-1.3545876724
53	C	-3.9199877312	0.3852762671	-0.7127643152
54	C	-5.3988525559	0.4490882673	-0.7649716890
55	H	3.0942621527	4.4251178485	1.6031474860
56	H	19.4179921686	-0.1870363654	0.7497114800
57	C	16.0969213299	0.5186390063	0.9073452845
58	C	9.5925612131	1.1646275382	0.7234413754
59	H	0.3521351747	-3.5129393114	-2.5943785084
60	H	0.5916391273	4.5093864749	1.4583611731
61	H	-18.5847437669	-1.7471402971	1.5416830154
62	H	-0.6578046941	2.6441050410	0.4623305454
63	C	11.0714018476	1.1706564492	0.8914466326
64	C	17.4853523455	0.6445700690	1.1210554482
65	C	13.8817253115	1.3359251312	1.2666464753
66	C	-16.6350630992	-1.1167235119	0.8979254592
67	C	-18.0334175847	-1.0858628676	0.8780366665
68	O	15.2466658104	1.4558545745	1.4589305555
69	H	1.8445339355	-2.6047087247	-2.9631668082
70	C	11.6596541329	2.1660526720	1.6594099405
71	C	7.6098222708	1.2742443630	-0.6864641475
72	C	-1.7786537054	1.1604887390	-1.5592304434
73	H	17.8546567885	1.4771307987	1.7115359085
74	C	8.9942693199	1.2183667183	-0.5466360004
75	C	-3.1921607771	1.1886987654	-1.5616667162
76	C	13.0536496921	2.2657897712	1.8551489924
77	N	-6.0600321054	-0.4226177944	0.1289480289
78	C	-8.0720450190	-1.2775784878	-0.7953395931
79	C	-8.0587675521	0.5224447933	0.9917241579
80	O	-7.4190137550	-2.0155396053	-1.5056271643
81	N	-7.4419081151	-0.3896705828	0.1055825028
82	O	-7.3947108199	1.2341969395	1.7182648899
83	C	-9.5554276085	-1.2266232375	-0.7924381444
84	C	-9.5425210188	0.5283720875	0.9540374904
85	C	-10.2666136387	-2.0587509152	-1.6416549417
86	C	-10.2396610820	-0.3368914872	0.0735730623
87	C	-10.2413279431	1.3857385175	1.7882821826
88	C	-11.6733486674	-2.0321755363	-1.6542399872
89	C	-11.6615519420	-0.3124059291	0.0594812100
90	C	-11.6481530585	1.4075665373	1.7729162819
91	C	-12.3661936008	-1.1733966689	-0.8166332991
92	C	-12.3534243734	0.5717515708	0.9225113922
93	C	-13.8547414752	-1.1637687658	-0.8420941530

94	C	-13.8417432800	0.6077046860	0.9240729942
95	H	-9.7168837727	-2.7294739324	-2.2935061538
96	O	-14.4982786817	-1.8899765993	-1.5810889678
97	H	-9.6819744803	2.0367884286	2.4518067997
98	N	-14.4962387750	-0.2696743019	0.0372911183
99	O	-14.4746688691	1.3535231217	1.6525687876
100	C	-15.9494855099	-0.2535365507	0.0320715017
101	H	-12.2370578485	-2.6812570916	-2.3158569210
102	H	11.0205994208	2.9199799813	2.1104896529
103	H	-12.2021268922	2.0753583226	2.4240462811
104	C	-18.7183666280	-0.2241967210	0.0245121917
105	H	13.4782569082	3.0670740983	2.4505982904
106	H	7.1606246412	1.3273192063	-1.6726538926
107	H	-19.8049880737	-0.2126463569	0.0215495427
108	H	9.6213876730	1.2450920080	-1.4330661484
109	C	-5.4722302084	-1.3233034767	1.0492664600
110	C	-16.6116549564	0.6239506080	-0.8372798088
111	C	-18.0105375461	0.6227323822	-0.8250945128
112	O	-6.1716778923	-2.0185844561	1.7609092303
113	C	-15.8511161853	1.5451770774	-1.7603172858
114	H	-18.5437857318	1.2958553438	-1.4916735287
115	H	-15.2088283665	2.2361038363	-1.2009031220
116	H	-15.2123475188	0.9847053983	-2.4535991740
117	H	-16.5432251711	2.1452427082	-2.3577702042
118	C	-3.9925083722	-1.3309211117	1.0605510605
119	C	-3.3400425239	-2.1681109004	1.9475446532
120	H	-3.9317792663	-2.7964165193	2.6048264370
121	C	-1.9338814917	-2.1837520132	1.9893229627
122	H	-1.4254090223	-2.8346269061	2.6945049820
123	C	-1.1967994922	-1.3781139013	1.1451306973
124	H	-0.1140547656	-1.3958543095	1.1976229668
125	O	-1.1924185285	2.0348260952	-2.4318562869
126	C	-0.1820177022	1.5633367239	-3.3307740400
127	H	-0.2906188841	2.1543016481	-4.2438657364
128	H	-0.3248378460	0.5022055350	-3.5609310127
129	H	0.8199678125	1.7168091366	-2.9192293300
130	H	-3.7019977033	1.8525417974	-2.2509995110

Table S3. Optimized cartesian coordinates for (R)-1-h₉.

(S)-1-h₉

Coordinates (Angstroms)

ATOM	X	Y	Z
1 C	17.4475492751	-1.7348908307	0.4157596817
2 C	18.3988117941	-0.7584104561	0.6446031257
3 C	18.0515751565	0.6175297370	0.7872092214
4 C	16.6717480335	0.9529257366	0.6810054414
5 C	15.7123688121	-0.0564053915	0.4446238925
6 C	16.0871814926	-1.3764790487	0.3159447150
7 C	18.9788188713	1.6668239536	1.0264080357
8 C	18.5336977517	2.9670751178	1.1500370600
9 C	17.1617779316	3.3006831816	1.0455022680
10 C	16.2430600744	2.2993790511	0.8133484350
11 C	14.3346873559	0.3301272277	0.3455613577
12 C	13.3723245058	-0.6791075337	0.1128919782
13 C	13.8101192750	-2.0253690700	0.0031291594
14 O	15.1490722085	-2.3638475260	0.0915262602
15 O	14.9034385863	2.6385697819	0.7165072235
16 C	13.9660633291	1.6513072205	0.4870169573
17 C	11.9893752169	-0.3446129856	0.0093429096
18 C	11.0472652202	-1.4037220693	-0.2181172140
19 C	11.5240049830	-2.7048787962	-0.3006010101
20 C	12.8922482857	-3.0329406261	-0.1942869281
21 C	12.6049329114	2.0052299597	0.4114034295
22 C	11.6504307121	1.0312654018	0.1823731182
23 C	9.5863189140	-1.1584891203	-0.3634120439
24 C	9.0756958417	-0.2777075887	-1.3322511746
25 C	7.7023752498	-0.1067355114	-1.4936929360
26 C	6.8174365157	-0.8170310671	-0.6854696566
27 C	7.3014025771	-1.6920909986	0.2844916947
28 C	8.6743732683	-1.8584342995	0.4430025136
29 N	5.3887179256	-0.6660113871	-0.8535014086
30 C	4.7621586781	-1.4877111055	-1.8189458784
31 C	3.2854262795	-1.3812765205	-1.9191900076
32 C	2.5678028776	-0.4900275506	-1.0801917529
33 C	3.2515254092	0.3278566438	-0.1530256495
34 C	4.7296037003	0.2562216743	-0.0178694306
35 O	5.4216974499	-2.2452732765	-2.5109689966
36 O	5.3530645094	0.9412485843	0.7778335736
37 C	1.1420384611	-0.4185973272	-1.1613057911
38 C	0.4346007230	0.4675083554	-0.2985590738
39 C	1.1468820722	1.2712749241	0.5947980634
40 C	2.5549961935	1.1978191745	0.6648481162
41 C	2.6132762276	-2.1766744476	-2.8279087264
42 C	1.2074975816	-2.1073226260	-2.9201577615
43 C	0.4879956644	-1.2558979757	-2.1084739331
44 C	-1.0577420273	0.5323103181	-0.3188832827
45 C	-1.7021744722	1.4455479032	-1.1558118252

46	C	-3.1110920305	1.5141474661	-1.1944879114
47	C	-3.8747327062	0.6798541851	-0.3992732154
48	C	-3.2619190434	-0.2547623298	0.4678266233
49	C	-1.8343579021	-0.3293464538	0.5103923371
50	C	-4.0392107839	-1.1158772009	1.2890261010
51	C	-3.4265053189	-2.0243837762	2.1315388757
52	C	-2.0197108700	-2.1010120213	2.1798699893
53	C	-1.2434490984	-1.2781852863	1.3916400881
54	C	-5.3488575157	0.7838084590	-0.4860238454
55	N	-6.0554585536	-0.1030774820	0.3554174820
56	C	-5.5166387885	-1.0590521727	1.2520664176
57	O	-6.2546813072	-1.7596046036	1.9178411796
58	O	-5.9433709589	1.5576339823	-1.2131537428
59	O	-0.8976794367	2.2348889404	-1.9166128412
60	C	-1.4936369051	3.2053563147	-2.7701812683
61	O	0.4042046792	2.0951401476	1.3827776473
62	C	1.0685484472	2.9254224701	2.3287594685
63	N	-7.4350343215	-0.0418599949	0.2880648814
64	C	-8.0503772911	-0.8970684392	-0.6539480970
65	C	-9.5323645822	-0.8271426577	-0.6917617471
66	C	-10.2295820994	0.0530770764	0.1735829007
67	C	-9.5469350892	0.8893599445	1.0925203258
68	C	-8.0652148510	0.8584508126	1.1767103480
69	C	-10.2294286060	-1.6319106921	-1.5782343926
70	C	-11.6348491093	-1.5873563794	-1.6290957796
71	C	-12.3403044195	-0.7372890410	-0.7931168807
72	C	-11.6500757973	0.0967495386	0.1196816061
73	C	-12.3550609353	0.9719459099	0.9812601774
74	C	-11.6637604089	1.7810248578	1.8681869488
75	C	-10.2583679551	1.7392339855	1.9237758091
76	C	-13.8274720935	-0.7105048362	-0.8575569077
77	N	-14.4826830471	0.1715738678	0.0239695510
78	C	-13.8425366912	1.0245799125	0.9442652295
79	O	-7.4137781582	1.5423911054	1.9403863999
80	O	-7.3863304395	-1.6243780043	-1.3651353746
81	O	-14.4863080466	1.7636507284	1.6701717773
82	O	-14.4587532940	-1.4137301641	-1.6285887437
83	H	13.2287803268	-4.0608672686	-0.2782598903
84	H	10.8147273477	-3.5074012834	-0.4817839433
85	H	10.6061877074	1.3215717718	0.1476655403
86	H	12.3200154972	3.0441649731	0.5444095140
87	H	17.7277436849	-2.7783561345	0.3112943256
88	H	19.4450214390	-1.0427783655	0.7201657738
89	H	20.0369729431	1.4350585457	1.1112450688
90	H	19.2481993232	3.7646734310	1.3338029655
91	H	16.8241839516	4.3267990303	1.1462052377
92	H	9.7608276840	0.2566750838	-1.9837265800
93	H	7.3153459614	0.5635634847	-2.2549578969

94	H	6.6032415652	-2.2364365495	0.9131753330
95	H	9.0510635008	-2.5316171771	1.2075068357
96	H	3.1244851560	1.8043788300	1.3583326663
97	H	3.1862713883	-2.8497640098	-3.4568973491
98	H	0.6877197155	-2.7358659067	-3.6374597085
99	H	-0.5935485540	-1.2175981218	-2.1857811257
100	H	-1.5453319798	-2.8169111242	2.8444997194
101	H	-4.0472344406	-2.6691643958	2.7446700507
102	H	-3.6299111919	2.2107281860	-1.8415862918
103	H	-9.6698752605	-2.2959764226	-2.2285579442
104	H	-12.1876952227	-2.2159803368	-2.3190106865
105	H	-12.2276333757	2.4423065219	2.5174649976
106	H	-9.7100120229	2.3676272989	2.6176122581
107	H	-0.6615671309	3.7180389509	-3.2550116658
108	H	-2.0871745086	3.9308496949	-2.2005969918
109	H	-2.1258632051	2.7360948454	-3.5341004328
110	H	0.2776681038	3.4769638426	2.8391938646
111	H	1.7472158141	3.6325006437	1.8361662373
112	H	1.6297952489	2.3324710646	3.0614662987
113	C	-15.9354808633	0.1958305600	-0.0122703144
114	C	-16.5758042831	1.1033784824	-0.8669327383
115	C	-15.7928075366	2.0518727685	-1.7422349671
116	C	-17.9746602124	1.1066726916	-0.8850872666
117	H	-18.4915017884	1.8025894620	-1.5411198600
118	C	-18.7030410777	0.2356850308	-0.0782102109
119	H	-19.7893125171	0.2512253056	-0.1042471108
120	C	-18.0395108006	-0.6552508471	0.7620667992
121	H	-18.6075101702	-1.3352368184	1.3917472836
122	C	-16.6420756964	-0.6920872765	0.8108531924
123	C	-15.9280367622	-1.6609388888	1.7224049060
124	H	-15.1387130339	1.5127210430	-2.4381779245
125	H	-15.1632655156	2.7231164956	-1.1456869805
126	H	-16.4699504255	2.6725081560	-2.3358858926
127	H	-15.2868386786	-1.1393352003	2.4429976006
128	H	-15.2954478879	-2.3551657409	1.1561325625
129	H	-16.6490947469	-2.2564324861	2.2895347957
130	H	-0.1618514242	-1.3475515026	1.4361573513

Table S4. Optimized cartesian coordinates for (S)-1-*h*₉.

2-h₉ Coordinates (Angstroms)

ATOM	X	Y	Z
1 C	16.2389988065	-1.2085745481	-0.2077704691
2 C	17.1878902191	-0.2059808573	-0.2793452660
3 C	16.8299273794	1.1742023226	-0.3170548233
4 C	15.4410854736	1.4855056127	-0.2778226179
5 C	14.4840152293	0.4491779158	-0.2063419279
6 C	14.8694027171	-0.8737099890	-0.1706059345
7 C	17.7547747970	2.2498694870	-0.3903938501
8 C	17.2985198747	3.5518039724	-0.4212719286
9 C	15.9175781122	3.8614500529	-0.3816585818
10 C	15.0010803418	2.8342174542	-0.3105513955
11 C	13.0970326691	0.8124965246	-0.1726387368
12 C	12.1384555570	-0.2234624144	-0.1015353339
13 C	12.5875519895	-1.5696994087	-0.0576249332
14 O	13.9335760099	-1.8865876429	-0.0994500212
15 O	13.6524933722	3.1509131251	-0.2718134021
16 C	12.7171148087	2.1380387642	-0.2036224147
17 C	10.7480550103	0.0871085227	-0.0637994574
18 C	9.8083244508	-0.9918796366	0.0109132387
19 C	10.2952627338	-2.2888995449	0.0684673186
20 C	11.6738815602	-2.5962097871	0.0326865914
21 C	11.3488373573	2.4716038626	-0.1555441801
22 C	10.3974970273	1.4700278653	-0.0848704088
23 C	8.3317252197	-0.7595181719	0.0504412720
24 C	7.6012106376	-0.3776154336	-1.0944429734
25 C	6.2142493683	-0.2425632951	-0.9742137100
26 C	5.5296733140	-0.4788391285	0.2250569668
27 C	6.2584542969	-0.8476047203	1.3740350935
28 C	7.6454380811	-0.9796441927	1.2522427729
29 C	4.0436434343	-0.3120409793	0.2473807510
30 N	-6.6617074487	-0.0871117428	0.0317899129
31 C	-7.1989954716	1.1549239433	0.4329140564
32 C	-8.6824337269	1.2765791978	0.4028423851
33 C	-9.4792319116	0.1863298400	-0.0227609054
34 C	-8.8909751873	-1.0360746132	-0.4270176042
35 C	-7.4118089135	-1.1949965597	-0.4147551044
36 C	-9.2815200505	2.4639669370	0.7924199155
37 C	-10.6826414153	2.5973324631	0.7704126737
38 C	-11.4830388262	1.5438361414	0.3577295753
39 C	-10.8943243035	0.3209156682	-0.0450258287
40 C	-11.6904827031	-0.7703307791	-0.4691171980
41 C	-11.0915596918	-1.9579032258	-0.8584565509
42 C	-9.6905937706	-2.0903281668	-0.8389550103
43 C	-12.9625439039	1.7029380639	0.3417135964
44 N	-13.7111299304	0.5942052784	-0.1030819200
45 C	-13.1733751428	-0.6498257526	-0.4960251677
46 O	-6.8637861581	-2.2227158779	-0.7751323587

47	O	-6.4756912410	2.0703474716	0.7842692923
48	O	-13.8970289769	-1.5688623336	-0.8389560481
49	C	-15.1546589828	0.7392745158	-0.1546807916
50	O	-13.5120837213	2.7327688242	0.6951322293
51	C	3.4947464923	0.9611792279	0.2088086728
52	C	2.1019230158	1.1671133462	0.2190926194
53	C	1.2359920549	0.0904167814	0.2636186679
54	C	1.7530819681	-1.2292276265	0.2908756845
55	C	3.1668059714	-1.4460190393	0.2771093727
56	C	0.8712316853	-2.3401449643	0.3248409869
57	C	1.3699699198	-3.6304160318	0.3363252085
58	C	2.7607386249	-3.8514261209	0.3063589431
59	C	3.6384023920	-2.7862875641	0.2747457507
60	C	-0.2275802471	0.3369229905	0.2716789316
61	N	-1.0566731497	-0.8064092500	0.2993107798
62	C	-0.5994632762	-2.1396610863	0.3439366068
63	O	-1.3907526830	-3.0683567764	0.3976357743
64	O	-0.7106143978	1.4572431884	0.2538963635
65	C	-2.4898471990	-0.5990471072	0.2617886624
66	C	-3.2513804196	-0.7151961922	1.4315379359
67	C	-4.6305922052	-0.5316386760	1.3077274606
68	C	-5.2197029881	-0.2407047259	0.0810921212
69	C	-4.4574502508	-0.1041530699	-1.0853433086
70	C	-3.0795013495	-0.2952408689	-0.9620516290
71	C	-15.9194129176	0.5629222038	1.0044927766
72	C	-17.3051238910	0.7184582179	0.8756971520
73	C	-17.8968008267	1.0286485001	-0.3460874637
74	C	-17.1231004237	1.1976762310	-1.5010089538
75	C	-15.7394902015	1.0490573728	-1.3807963998
76	C	5.5898402420	-1.0765189868	2.7111253811
77	C	8.2689661013	-0.1523716750	-2.4318897687
78	C	-15.2913606761	0.2318866574	2.3353903073
79	C	-17.7635765474	1.5187317461	-2.8311611111
80	C	-5.0808412467	0.2132739417	-2.4212502578
81	C	-2.6294808604	-1.0459030744	2.7643896152
82	H	16.5283274190	-2.2543837020	-0.1794858149
83	H	18.2411927950	-0.4720913366	-0.3079015850
84	H	18.8198435370	2.0373044837	-0.4218104211
85	H	18.0112582311	4.3699210677	-0.4771319913
86	H	15.5718029689	4.8895139374	-0.4063840345
87	H	12.0188211331	-3.6240983751	0.0710325439
88	H	9.5852615723	-3.1089357649	0.1317488983
89	H	9.3475263123	1.7404292283	-0.0328548659
90	H	11.0587329631	3.5175765206	-0.1685301742
91	H	8.2228109938	-1.2577071673	2.1308429273
92	H	5.6374337608	0.0341247450	-1.8537879620
93	H	4.1597060550	1.8194832807	0.1795617311
94	H	1.6856988906	2.1689789140	0.1948086659

95	H	3.1420873980	-4.8683904838	0.3037284137
96	H	0.6681482981	-4.4574409110	0.3619468023
97	H	-2.4475344558	-0.2074632570	-1.8408175044
98	H	-5.2627547834	-0.6206601743	2.1864888851
99	H	-9.2133519982	-3.0156829381	-1.1435479711
100	H	-11.7247431077	-2.7788973905	-1.1776567537
101	H	-8.6483949250	3.2843249520	1.1134612214
102	H	-11.1590379521	3.5233938711	1.0741983013
103	H	-15.1008663835	1.1732882006	-2.2512005937
104	H	-18.9775269834	1.1395286334	-0.4033115290
105	H	-17.9302390061	0.5919175915	1.7563413867
106	H	4.7088835600	-2.9620638588	0.2414674872
107	H	4.9571173014	-0.2278118206	2.9955067481
108	H	6.3367414518	-1.2182586100	3.4979741818
109	H	4.9445162717	-1.9634368845	2.7024520535
110	H	8.8909949801	-1.0087279264	-2.7162848522
111	H	8.9269716201	0.7248979684	-2.4193180398
112	H	7.5234146608	0.0018706665	-3.2179373251
113	H	-5.7028355985	1.1146625473	-2.3728422750
114	H	-5.7136727762	-0.6124845956	-2.7675856034
115	H	-4.3083483820	0.3824725330	-3.1768905609
116	H	-2.2492885833	-2.0740594439	2.7707459835
117	H	-3.3636218934	-0.9506510898	3.5697020181
118	H	-1.7903299813	-0.3791517595	2.9937817489
119	H	-14.6693244671	-0.6692519090	2.2773927887
120	H	-16.0620546533	0.0555260727	3.0915518177
121	H	-14.6568904844	1.0529112394	2.6901940205
122	H	-17.0101458972	1.7247154823	-3.5977846523
123	H	-18.4179315116	2.3957306539	-2.7593981379
124	H	-18.3799122012	0.6840476547	-3.1886897819

Table S5. Optimized cartesian coordinates for 2-*h*₉.

θ	I_{CISS}	I_S	I_{13}
0	$\frac{1}{4} \cos^2 \phi$	$\frac{1}{2} \sin^2 \phi \cos^2 \phi$	$\frac{1}{4} \cos^2 \phi (1 - \cos 2\phi \cos 2\chi)$
90	$-\frac{1}{8} \cos 2\phi \cos^2 \phi$	$\frac{1}{2} \sin^2 \phi \cos^2 \phi$	$\frac{1}{4} \cos^2 \phi (\cos 2\chi - \cos 2\phi \cos^2 \chi)$

Table S6. Summary of the different intensities for transition 1↔3 assuming 100% CISS, pure singlet and partial CISS efficiency (see Eqs. S16, S15, S13).

g_{NDI}	(2.0034, 2.0041, 2.0044)
g_{PXX}	(2.0031, 2.0044, 2.0046)
r_{DA}	2.5 nm
σ_D	0.35 nm
a_{NDI}	6.3 MHz
a_{PXX}	10 MHz
ΔB_0	0.4 mT

Table S7. Summary of the parameters used for the simulations of Fig. 4, where σ_D is the width of the gaussian distribution of DA distances (used to compute $D(\theta)$, Eq. S2) and ΔB_0 is the additional gaussian broadening used to convolute the spectra and accounting for inhomogeneous broadening of the remaining parameters. Parameters are given in the laboratory frame, with the magnetic field along z.

References and Notes

50. A. Sciutto *et al.*, Customizing photoredox properties of PXX-based dyes through energy level rigid shifts of frontier molecular orbitals. *Chem. - Eur. J.* **24**, 4382-4389 (2018).
51. J. L. Sessler *et al.*, A rigid chlorin-naphthalene diimide conjugate. A possible new noncovalent electron transfer model system. *J. Org. Chem.* **63**, 7370-7374 (1998).
52. R. M. Young *et al.*, Ultrafast conformational dynamics of electron transfer in exbox⁴⁺⊂perylene. *J. Phys. Chem. A* **117**, 12438-12448 (2013).
53. D. Gosztola, M. P. Niemczyk, W. Svec, A. S. Lukas, M. R. Wasielewski, Excited doublet states of electrochemically generated aromatic imide and diimide radical anions. *J. Phys. Chem. A* **104**, 6545-6551 (2000).
54. S. Stoll, A. Schweiger, Easyspin, a comprehensive software package for spectral simulation and analysis in EPR. *J. Magn. Reson.* **178**, 42-55 (2006).
55. C. E. Tait, M. D. Krzyaniak, S. Stoll, Computational tools for the simulation and analysis of spin-polarized EPR spectra. *J. Magn. Reson.* **349**, 107410 (2023).
56. Y. Shao *et al.*, Advances in molecular quantum chemistry contained in the Q-Chem 4 program package. *Mol. Phys.* **113**, 184-215 (2015).
57. P. J. Hore, in *Advanced EPR in biology and biochemistry*, A. J. Hoff, Ed. (Elsevier, Amsterdam, 1989), pp. 405-440.
58. A. Weller, Photoinduced electron transfer in solution: Exciplex and radical ion pair formation free enthalpies and their solvent dependence. *Z. Phys. Chem.* **133**, 93-99 (1982).
59. H. Mao, R. M. Young, M. D. Krzyaniak, M. R. Wasielewski, Controlling the dynamics of three electron spin qubits in a donor-acceptor-radical molecule using dielectric environment changes. *J. Phys. Chem. Lett.* **12**, 2213-2218 (2021).
60. G. L. Closs, J. R. Miller, Intramolecular long-distance electron transfer in organic molecules. *Science* **240**, 440-447 (1988).